Computer Methods in Applied Mechanics and Engineering 459 (2026) 119078

Contents lists available at ScienceDirect

Comput. Methods Appl. Mech. Engrg.

journal homepage: www.elsevier.com/locate/cma

Dual-horizon peridynamics with variational damage for hydro-mechanically coupled hydraulic fracturing in porous media

Yongzheng Zhang [a,b,c,1], Jidong Zhao [c], Gang Wang [b,d,*], Xuxu Yang [b], Timon Rabczuk [e,**]

[a] Jiangsu Key Laboratory of Oil and Gas Storage and Transportation Technology, Changzhou University, Changzhou, 213164, China
[b] Department of Civil Engineering, Shandong University of Science and Technology, Qingdao, 266590, China
[c] Department of Civil and Environmental Engineering, Hong Kong University of Science and Technology, 999077, Hong Kong, China
[d] Department of Civil Engineering, Fujian University of Technology, Fuzhou, 350118, China
[e] Institute of Structural Mechanics, Bauhaus-University Weimar, Weimar, 99423, Germany

ARTICLE INFO

Keywords:
Dual-horizon peridynamics
Hydro-mechanical coupling
Poroelasticity
Variational damage
Porous media

ABSTRACT

Hydraulic fracturing in fluid-saturated porous media constitutes a challenging multiphysics problem involving the coupled evolution of fluid flow, solid deformation, and fracture propagation. This work presents a novel computational framework that integrates dual-horizon non-ordinary state-based peridynamics (DH-NOSBPD) with variational damage mechanics and Biot's poroelasticity theory for simulating hydraulic fracture propagation in brittle porous materials. The dual-horizon formulation permits spatially varying discretization while rigorously preserving linear and angular momentum balance, thereby overcoming a fundamental constraint of conventional peridynamic methods. A dynamically consistent energy functional is constructed that couples mechanical deformation, pore pressure diffusion, and damage evolution, with governing equations derived systematically through variational principles. By employing an energetically motivated damage variable, the proposed approach obviates phenomenological bond-breaking criteria, enabling autonomous crack nucleation, propagation, branching, and coalescence without recourse to explicit fracture tracking algorithms. A stabilized formulation is adopted to suppress zero-energy modes while preserving computational efficiency. The resulting coupled system is solved via an adaptive staggered scheme that combines forward Euler integration for fluid diffusion with adaptive dynamic relaxation for quasi-static mechanical equilibrium. The framework is validated against analytical solutions and benchmark problems, including Terzaghi's consolidation, five-spot well flow, pressure-driven fracture initiation, and interaction with natural discontinuities, demonstrating its accuracy, robustness, and capability to model complex hydraulic fracturing scenarios.

1. Introduction

Hydraulic fracturing in fluid-saturated porous media constitutes a fundamental multiphysics problem with far-reaching implications for geotechnical engineering, subsurface energy extraction, and enhanced oil recovery [1,2]. The phenomenon involves intricate interactions among fluid flow, solid deformation, and fracture propagation, operating across disparate length and time scales [3,4]. Traditional continuum mechanics formulations encounter fundamental difficulties when treating the displacement

* Corresponding author at: Department of Civil Engineering, Shandong University of Science and Technology, Qingdao, 266590, China
** Corresponding author.
E-mail addresses: wanggang1110@gmail.com (G. Wang), timon.rabczuk@uni-weimar.de (T. Rabczuk).
[1] Formerly at affiliation b.

https://doi.org/10.1016/j.cma.2026.119078
Received 16 December 2025; Received in revised form 30 March 2026; Accepted 10 May 2026
Available online 18 May 2026

discontinuities inherent to fracture processes, particularly under complex hydro-mechanical coupling conditions where pore pressure evolution, effective stress redistribution, and permeability changes occur simultaneously [5,6].

Significant methodological advances have been achieved in computational fracture mechanics to circumvent these limitations. Extended finite element methods (XFEM) incorporate discontinuous enrichment functions to represent crack surfaces independently of mesh topology, thereby enabling crack propagation without remeshing [7,8]. Phase-field methods (PFM) regularize sharp crack surfaces through a diffuse damage variable governed by an auxiliary partial differential equation, naturally accommodating complex topological changes including branching and coalescence [9–11]. Cohesive zone models (CZM) introduce traction-separation relationships along potential fracture surfaces, providing physical representation of the fracture process zone [12,13]. Discrete element methods (DEM) and discrete fracture network (DFN) approaches directly represent rock as assemblies of interacting blocks or particles, naturally handling large deformations and complex fracture patterns at substantial computational cost [14,15]. Despite these advances, challenges persist regarding the treatment of arbitrary crack paths, fracture pattern complexity, and the seamless coupling between fluid transport and evolving discontinuities [16].

Peridynamics, introduced by Silling [17], provides an alternative nonlocal continuum mechanics framework particularly well-suited for fracture analysis. The distinguishing feature of peridynamics lies in its integral formulation of the equations of motion, which replaces spatial derivatives with integral operators over finite neighborhoods termed horizons [18]. This formulation remains valid regardless of material continuity, enabling natural treatment of crack nucleation, propagation, branching, and coalescence without external criteria [19]. The nonlocal nature inherently captures material length scales, providing physical representation of process zones and size effects that emerge from the constitutive model rather than requiring separate treatment [20]. However, standard peridynamic formulations typically employ uniform horizon sizes throughout the computational domain to simplify numerical implementation, which limits adaptive discretization refinement and efficient handling of multi-scale problems [21,22]. The dual-horizon peridynamics (DH-PD) formulation proposed by Ren et al. [23] addresses this limitation by permitting each material point to possess its own characteristic interaction radius while rigorously maintaining fundamental conservation principles.

The field of peridynamic modeling for fluid-driven fracture has witnessed substantial methodological development through multiple coupling frameworks. State-based poroelastic implementations address multi-scale transport phenomena, incorporating both matrix permeability and fracture-specific flow mechanisms [24]. These formulations draw upon nonlocal representations of pressure-driven convection in permeable solids [25], establishing consistency with continuum transport theory while accommodating displacement discontinuities. Coupled frameworks treating simultaneous mechanical response and fluid infiltration have enabled prediction of crack evolution in spatially variable geological materials [26]. Complementary efforts have investigated partitioned numerical schemes, wherein nonlocal discretization applies selectively to anticipated damage zones while conventional finite element approximation governs surrounding continuous regions [27–29]. Extensions to naturally fractured formations demonstrate applicability across realistic reservoir configurations [30,31].

Current peridynamic hydraulic fracturing models predominantly employ displacement-based or energy-density thresholds to trigger bond failure [24,26,27]. Although computationally efficient and physically transparent, this criterion-driven paradigm differs fundamentally from the energy minimization principles underlying contemporary phase-field fracture theory. Variational approaches to fracture mechanics, pioneered by Francfort and Marigo [32], reformulate crack propagation as an energy minimization problem over all admissible displacement and crack configurations, thereby providing a unified framework that encompasses crack initiation, propagation, branching, and arrest without recourse to external criteria. The total energy functional comprises elastic strain energy in the uncracked domain and fracture surface energy proportional to crack area, with Griffith's criterion emerging naturally from the first-order optimality conditions [33]. Regularization through gradient damage models or phase-field methods enables practical numerical implementation while preserving theoretical rigor [10]. The resulting variational damage formulation exhibits several advantageous features, including dynamic consistency, natural nucleation of cracks without prescribed initiation sites, and stable numerical behavior during crack propagation [34,35]. Extensions of variational fracture theory to coupled problems—including thermal effects [36], dynamic loading [11], and hydraulic fracturing [37–39]—have demonstrated the generality and robustness of this framework.

Recent work by Ren et al. [40] introduced variational damage concepts into DH-PD for dynamic fracture problems, demonstrating that damage evolution can be derived from energy minimization principles rather than imposed through bond-breaking rules. This development established the feasibility of integrating variational damage theory with nonlocal peridynamic formulations, achieving dynamically consistent damage evolution without requiring gradient terms in the damage field. However, extension to hydraulic fracturing introduces substantial additional complexity due to the pressure-dependent effective stress, bidirectional hydro-mechanical coupling, evolving permeability in damaged regions, and fluid flow within propagating fractures.

This study presents a unified computational methodology that integrates DH-NOSBPD with variational damage formulations for modeling hydraulic fracturing in brittle porous materials. The principal contributions of this investigation comprise:

(1) A dual-horizon peridynamic formulation for hydro-mechanically coupled problems is rigorously developed, wherein both mechanical equilibrium and pore pressure diffusion equations are derived using consistent nonlocal gradient operators. This formulation inherently accommodates non-uniform spatial discretization while ensuring strict adherence to fundamental conservation principles.

(2) The integration of variational damage theory within the dual-horizon framework provides an energy-based alternative to the conventional bond-breaking criterion, enabling damage evolution derived from variational principles. Unlike phase-field methods requiring gradient terms and fine mesh resolution for diffuse crack regularization, the present formulation achieves damage evolution without higher-order derivatives—the nonlocal operators inherently provide regularization through the horizon parameter. This gradient-free approach yields sharper crack representations while maintaining thermodynamic consistency.

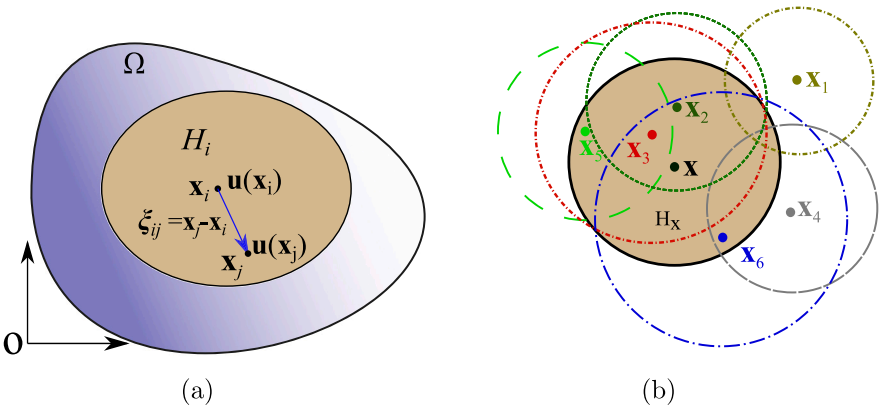

Fig. 1. (a) Deformed body configuration representation. (b) Illustration of dual-horizon concept, $\mathcal{H}_i = \{\mathbf{x}_2, \mathbf{x}_3, \mathbf{x}_5, \mathbf{x}_6\}$, $\mathcal{H}'_i = \{\mathbf{x}_2, \mathbf{x}_3, \mathbf{x}_6\}$.

(3) A unified treatment of pore fluid transport through intact porous media and evolving fracture networks is achieved by formulating the pressure diffusion equation with nonlocal operators consistent with the mechanical formulation. The damage-dependent permeability model enables smooth transitions between matrix and fracture flow regimes.
(4) An adaptive staggered solution algorithm is developed that combines forward Euler integration for fluid diffusion with adaptive dynamic relaxation for quasi-static mechanical equilibrium. Damage evolution is obtained through direct evaluation of variational optimality conditions, obviating the computationally intensive iterative solutions typically required by conventional phase-field approaches.

The remainder of this paper is organized as follows. Section 2 establishes the mathematical foundations of DH-PD, encompassing the governing equations, constitutive relationships, and hourglass mode stabilization techniques. Section 3 develops the variational formulation for hydraulic fracturing, derives the complete energy functional, and demonstrates its thermodynamic consistency; furthermore, the coupled hydro-mechanical governing equations arising from variational principles are presented, including the damage evolution laws, effective stress formulations, and permeability models. Section 4 details the numerical implementation, addressing spatial discretization, temporal integration schemes, and staggered solution algorithms. Section 5 provides comprehensive validation against analytical solutions and presents representative numerical examples that demonstrate the capabilities of the proposed framework for modeling complex fracturing scenarios. Finally, Section 6 summarizes the key findings and outlines potential directions for future research.

2. DH-NOSBPD theory

We examine a solid continuum occupying a spatial domain ($\Omega \subset \mathbb{R}^d$ for d-dimensional analysis) as illustrated in Fig. 1(a). The continuum undergoes spatial discretization through a finite assembly of material points, wherein each point represents a discrete material volume element. The position vector $\mathbf{x}_i$ denotes the spatial location of material point i within the undeformed configuration. The DH-PD framework introduces a distinctive feature whereby two separate neighborhood regions are defined for each material point, establishing a fundamental departure from classical peridynamic theory [23].

For material point i, the horizon region $\mathcal{H}_i$ is defined as:

$$\mathcal{H}_i = \left\{\mathbf{x}_j \in \Omega \mid \|\mathbf{x}_j - \mathbf{x}_i\| \leq \delta_i\right\} \tag{1}$$

wherein δ_i designates the horizon size associated with point i, while $\|\cdot\|$ signifies the Euclidean norm.

This region encompasses the complete set of material points located within a neighborhood of radius δ_i centered at point i, thereby establishing the spatial extent of nonlocal interaction influences originating from that point. The dual-horizon formulation permits individual specification of horizon radii δ_i for each material point, facilitating straightforward implementation of spatially varying discretizations and adaptive refinement strategies [23,41].

The complementary dual-horizon region $\mathcal{H}'_i$ associated with material point i is defined as:

$$\mathcal{H}'_i = \left\{\mathbf{x}_j \in \Omega \mid \mathbf{x}_i \in \mathcal{H}_j\right\} = \left\{\mathbf{x}_j \in \Omega \mid \|\mathbf{x}_i - \mathbf{x}_j\| \leq \delta_j\right\} \tag{2}$$

This dual-horizon region consists of the collection of material points whose respective horizon regions contain point i. The conceptual distinction is significant: whereas $\mathcal{H}_i$ derives exclusively from the horizon parameter δ_i of point i, the dual-horizon $\mathcal{H}'_i$ emerges from the collective horizon parameters δ_j of all remaining material points j [23].

Fig. 1(b) illustrates both the horizon and dual-horizon constructs. Under uniform horizon conditions ($\delta_i = \delta$ throughout the domain), both regions become identical ($\mathcal{H}'_i = \mathcal{H}_i$), thereby reducing to the traditional constant-horizon peridynamic formulation.

The equation of motion governing DH-NOSBPD emerges through systematic integration of both horizon constructs. The resulting formulation reads:

$$\rho\ddot{\boldsymbol{u}}(\boldsymbol{x}_i,t)=\int_{\mathcal{H}_i}\boldsymbol{f}(\boldsymbol{u}_{ij},\boldsymbol{\xi}_{ij})dV_j-\int_{\mathcal{H}_i'}\boldsymbol{f}(-\boldsymbol{u}_{ij},-\boldsymbol{\xi}_{ij})dV_j+\boldsymbol{b}(\boldsymbol{x}_i,t), \tag{3}$$

where $\boldsymbol{f}(\boldsymbol{u}_{ij},\boldsymbol{\xi}_{ij})$ represents the pairwise force density function associated with bond deformation, with $\boldsymbol{\xi}_{ij}=\boldsymbol{x}_j-\boldsymbol{x}_i$ denoting the bond vector satisfying $\boldsymbol{\xi}_{ji}=-\boldsymbol{\xi}_{ij}$.

2.1. Constitutive correspondence

The key advantage of NOSBPD lies in its ability to incorporate classical constitutive models through the correspondence framework [20], which bridges nonlocal peridynamic force states and classical stress measures.

This capability facilitates the direct integration of sophisticated classical material models into the nonlocal framework. Rooted in the multi-physical and non-orthogonal geotechnical plasticity theory [42–44], the elasto-plasticity damage model proposed by Zhou et al. [45] and Lu et al. [43] accurately captures the complex mechanical behaviors of the concrete material, including strain softening, stiffness degradation, dilatancy/contraction, and strain rate effect, all with a streamlined parameter set, rendering it suited for the high-fidelity simulation of concrete structures under extreme seismic, impact, and blast loads. While the current investigation focuses on brittle porous media, such advanced formulations can be readily accommodated within the NOSBPD architecture for complex dynamic applications.

The nonlocal deformation gradient at point $\boldsymbol{x}_i$ is

$$\boldsymbol{F}_i=\int_{\mathcal{H}_i}\omega(\boldsymbol{\xi}_{ij})(\boldsymbol{y}_j-\boldsymbol{y}_i)\otimes\boldsymbol{\xi}_{ij}\,dV_j\cdot\boldsymbol{K}_i^{-1}=\boldsymbol{I}+\nabla\boldsymbol{u}_i, \tag{4}$$

where $\boldsymbol{y}=\boldsymbol{x}+\boldsymbol{u}$ denotes the deformed position. For hyperelastic materials with strain energy $W(\boldsymbol{F})$, the first Piola–Kirchhoff stress is

$$\boldsymbol{P}_i=\left.\frac{\partial W}{\partial\boldsymbol{F}}\right|_{\boldsymbol{F}=\bar{\boldsymbol{F}}_i}. \tag{5}$$

The transformation $\boldsymbol{P}=J\boldsymbol{\sigma}\boldsymbol{F}^{-T}$ relates the first Piola–Kirchhoff stress to the Cauchy stress $\boldsymbol{\sigma}$, with $J=\det(\boldsymbol{F})$. Under small deformations ($\boldsymbol{F}\approx\boldsymbol{I}$, $J\approx 1$):

$$\boldsymbol{P}\approx\boldsymbol{\sigma}. \tag{6}$$

The force density derives from the stress tensor as [20]

$$\boldsymbol{f}_{ij}=\omega(\boldsymbol{\xi}_{ij})\boldsymbol{P}_i\boldsymbol{K}_i^{-1}\boldsymbol{\xi}_{ij}, \tag{7}$$

This expression establishes the connection between peridynamic forces and classical stress, and naturally accommodates anisotropic behavior.

2.2. Nonlocal operators and stabilization

In the state-based peridynamic setting, the nonlocal counterpart of the gradient of a vector field $\boldsymbol{u}$, computed at material point $\boldsymbol{x}_i$ with respect to its horizon $\mathcal{H}_i$, takes the form [20]

$$\bar{\nabla}\boldsymbol{u}_i:=\int_{\mathcal{H}_i}\omega(\boldsymbol{\xi}_{ij})\boldsymbol{u}_{ij}\otimes\boldsymbol{\xi}_{ij}dV_j\cdot\boldsymbol{K}_i^{-1} \tag{8}$$

where $\omega(\boldsymbol{\xi}_{ij})$ constitutes a positive-valued influence function serving two essential roles: amplifying contributions from nearby neighbors and maintaining proper dimensional consistency [46].

The shape tensor $\boldsymbol{K}_i$ emerges from the integral formulation

$$\boldsymbol{K}_i=\int_{\mathcal{H}_i}\omega(\boldsymbol{\xi}_{ij})\boldsymbol{\xi}_{ij}\otimes\boldsymbol{\xi}_{ij}dV_j. \tag{9}$$

Suppression of the zero-energy deformation modes that are endemic to correspondence-based NOSBPD is achieved through a penalty-type stabilization functional defined at each material point $\boldsymbol{x}_i$ [47,48]:

$$\psi_i^{hg}=\frac{p_{hg}}{m_{\boldsymbol{K}_i}}\int_{\mathcal{H}_i}\omega(\boldsymbol{\xi}_{ij})(\bar{\nabla}\boldsymbol{u}_i\cdot\boldsymbol{\xi}_{ij}-\boldsymbol{u}_{ij})\cdot(\bar{\nabla}\boldsymbol{u}_i\cdot\boldsymbol{\xi}_{ij}-\boldsymbol{u}_{ij})dV_j, \tag{10}$$

where p_{hg} specifies the stabilization penalty parameter and $m_{\boldsymbol{K}_i}=\int_{\mathcal{H}_i}\omega(\boldsymbol{\xi}_{ij})\boldsymbol{\xi}_{ij}\cdot\boldsymbol{\xi}_{ij}dV_j$ provides the normalization scalar.

Applying variational principles to the hourglass control functional ψ_i^{hg} [46] yields the stabilization force contribution for each bond interaction as

$$\boldsymbol{\mathcal{F}}_{ij}^{hg}=\frac{2p_{hg}}{m_{\boldsymbol{K}_i}}\omega(\boldsymbol{\xi}_{ij})(\boldsymbol{u}_{ij}-\bar{\nabla}\boldsymbol{u}_i\cdot\boldsymbol{\xi}_{ij}) \tag{11}$$

In all numerical examples presented in this work, the hourglass stabilization parameter is set to $p_{hg}=\mu$, where μ is the shear modulus of the material.

Invoking the small deformation hypothesis, the Cauchy stress tensor $\boldsymbol{\sigma}$ coincides with the first Piola–Kirchhoff stress measure. The stabilized equation of motion therefore takes the form

$$\rho\ddot{\boldsymbol{u}}_i = \int_{\mathcal{H}_i} (\omega(\boldsymbol{\xi}_{ij})\boldsymbol{\sigma}_i \boldsymbol{K}_i^{-1}\boldsymbol{\xi}_{ij} + \boldsymbol{\mathcal{T}}_{ij}^{hg})dV_j - \int_{\mathcal{H}_i'} (\omega(\boldsymbol{\xi}_{ji})\boldsymbol{\sigma}_j \boldsymbol{K}_j^{-1}\boldsymbol{\xi}_{ji} + \boldsymbol{\mathcal{T}}_{ji}^{hg})dV_j + \boldsymbol{b}. \tag{12}$$

This formulation connects the dual-horizon framework with classical continuum mechanics: the Cauchy stress $\boldsymbol{\sigma}_i$ computed from any constitutive model is projected onto peridynamic force states, while the dual-horizon structure ensures proper force balance with variable horizon sizes.

3. Hydro-mechanical variational damage model in DH-NOSBPD

This section details how variational damage mechanics is embedded into the DH-NOSBPD formulation of Section 2. The discussion covers the foundational principles of energy-based damage theory, the derivation of damage evolution equations from energy minimization, and the resulting modified field equations that avoid explicit bond-rupture procedures. The formulation draws on recent progress in variational fracture theory [10,32,33] and DH-PD [23], extending the preliminary work of Ren et al. [34].

3.1. Poroelastic theory and effective stress principle

For fluid-saturated porous media, we adopt Biot's theory of poroelasticity adapted to the peridynamic framework [3,4]. The total stress state includes contributions from the solid skeleton and pore fluid pressure:

$$\boldsymbol{\sigma}^{por} = \boldsymbol{\sigma}^{e} - \alpha p\mathbf{I} \tag{13}$$

where p denotes the pore fluid pressure, α is the Biot coefficient, and $\mathbf{I}$ represents the identity tensor.

The Biot coefficient quantifies the effective stress response to pore pressure changes and depends on the bulk moduli of the porous medium and the solid matrix:

$$\alpha = 1 - \frac{K_d}{K_s} \tag{14}$$

where K_d denotes the drained bulk modulus of the porous medium and K_s represents the bulk modulus of the solid constituent material.

The effective stress tensor $\boldsymbol{\sigma}^e$ relates to the strain tensor through the elastic constitutive relation:

$$\boldsymbol{\sigma}^{e} = \lambda \mathrm{tr}(\boldsymbol{\varepsilon})\mathbf{I} + 2\mu\boldsymbol{\varepsilon} \tag{15}$$

Combining Eqs. (13) and (15), the total stress becomes:

$$\boldsymbol{\sigma}^{por} = \lambda \mathrm{tr}(\boldsymbol{\varepsilon})\mathbf{I} + 2\mu\boldsymbol{\varepsilon} - \alpha p\mathbf{I} \tag{16}$$

3.2. Variational damage theory

Traditional continuum fracture theory characterizes material failure through geometric singularities accompanied by dissipative mechanisms, wherein Griffith's energy balance principle [49,50] provides the fundamental criterion. The energy-based variational framework for brittle failure, established through the seminal work of Francfort and Marigo [32], recasts this equilibrium condition as a global minimization principle encompassing all kinematically admissible discontinuity patterns.

For a bounded domain Ω occupied by a solid containing a discontinuity set Γ, the aggregate energy functional incorporates two distinct contributions: the stored elastic deformation energy and the dissipative fracture surface energy:

$$\mathcal{E}[\boldsymbol{u}, \Gamma] = \int_{\Omega\setminus\Gamma} W(\boldsymbol{\varepsilon}(\boldsymbol{u}))\, dV + G_c \int_{\Gamma} d\Gamma \tag{17}$$

where $\Omega\setminus\Gamma$ denotes the intact (uncracked) portion of the body, $W(\boldsymbol{\varepsilon})$ is the elastic strain–energy density, and the second contribution corresponds to the Griffith-type fracture surface energy, with G_c denoting the critical energy-release rate.

Direct numerical minimization of Eq. (17) is nontrivial, primarily because the crack set Γ represents an *a priori* unknown discontinuity. To circumvent this difficulty, a regularized variational framework is adopted by introducing a scalar crack (damage) variable $s(\mathbf{x}) \in [0, 1]$, which varies continuously from the intact state ($s = 0$) to the fully degraded state ($s = 1$) within a characteristic length ℓ [10,33]. In this setting, the sharp crack topology is replaced by a spatially distributed damage band, and the corresponding fracture surface contribution is approximated through a regularized functional of the form:

$$\int_{\Gamma} d\Gamma \approx \int_{\Omega} \gamma_\ell(s, \nabla s)\, dV \tag{18}$$

where $\gamma_\ell(s, \nabla s)$ is the crack surface density function per unit volume.

The widely adopted AT2 model uses the crack density function [10,51]:

$$\gamma_\ell(s, \nabla s) = \frac{1}{2\ell} s^2 + \frac{\ell}{2}|\nabla s|^2 \tag{19}$$

This formulation involves the damage-field gradient ∇s, which provides a regularization by replacing the sharp crack surface with a diffuse transition zone whose characteristic thickness scales with ℓ. In the limiting case $\ell \to 0$, the regularized representation approaches the sharp-interface description, and the crack-surface density functional satisfies $\int_\Omega \gamma_\ell(s, \nabla s)\, dV \to \int_\Gamma d\Gamma$ as established in [33].

A key feature of the variational damage model [34] presented here is that, unlike phase-field models which include a gradient term in the crack surface density, the current formulation employs a simpler representation that depends only on the damage field itself:

$$\gamma_\ell(s) = \frac{1}{\ell}\Gamma(s) = \frac{1}{\ell}s^{m+1} \quad (m > 0) \overset{m=1}{\Longrightarrow} \gamma_\ell(s) = \frac{1}{\ell}s^2 \tag{20}$$

This choice leads to a sharper representation of the crack path with a width proportional to the length scale ℓ, in contrast to phase-field models where the crack width scales with $\sqrt{\ell}$. The absence of the gradient term simplifies the governing equation for damage evolution and reduces computational cost.

Remark 1 (*Justification of the Normalization Factor* $1/\ell$)**.** It is important to note that the normalization factor $1/\ell$ in Eq. (20) differs from the factor $1/2\ell$ appearing in the classical AT2 crack density function (Eq. (19)). In the full AT2 formulation, the local term $s^2/2\ell$ and the gradient term $(\ell/2)|\nabla s|^2$ each contribute one-half of the total fracture energy per unit crack area [33,51]. When the gradient term is omitted—as in the present variational damage model where the nonlocal peridynamic operators provide regularization through the horizon parameter δ—the local term must carry the entire fracture energy dissipation. This necessitates a normalization factor of $1/\ell$ rather than $1/2\ell$.

The correctness of this choice can be verified through the asymptotic property of the variational damage functional [34,35]. Substituting the optimal damage field $s = \psi_e^+/(\psi_e^+ + G_c/\ell)$ into the total energy density yields:

$$g(s)\psi_e^+ + \frac{G_c}{\ell}s^2 = \frac{G_c\psi_e^+}{\ell\psi_e^+ + G_c} \xrightarrow{\psi_e^+ \to \infty} \frac{G_c}{\ell} \tag{21}$$

This energy saturation property demonstrates that, at a fully damaged material point, the energy density converges to G_c/ℓ regardless of the applied strain magnitude. For a localized damage band of characteristic width proportional to ℓ (as controlled by the nonlocal horizon δ), the total dissipated fracture energy per unit crack area is:

$$\Gamma_f = \int_{\text{damage band}} \frac{G_c}{\ell}\, dx \approx \frac{G_c}{\ell} \times \ell = G_c \tag{22}$$

thereby ensuring consistency with Griffith's criterion. This confirms that the normalization factor $1/\ell$ is not merely transferred from the classical AT2 derivation but arises naturally from the energy structure of the variational damage functional in the gradient-free peridynamic setting [34,35].

The elastic strain energy density in the presence of damage is modified by a monotonically decreasing degradation function $g(s) = (1-s)^{m+1}, (m > 0)$, satisfying $g(0) = 1$ (undamaged) and $g(1) = 0$ (fully damaged). A common choice is quadratic degradation [10]:

$$g(s) = (1-s)^2 \tag{23}$$

The degraded elastic strain energy density then reads:

$$\psi(\boldsymbol{\varepsilon}, s) = g(s)\psi_e^+(\boldsymbol{\varepsilon}) + \psi_e^-(\boldsymbol{\varepsilon}) \tag{24}$$

Here, the elastic energy has been decomposed into tensile and compressive parts, ψ_e^+ and ψ_e^-, respectively. The degradation function affects only the tensile part of the energy, allowing compressive stresses to be transmitted across crack surfaces.

A small residual stiffness parameter (typically $k = 10^{-9}$) is introduced to prevent complete loss of stiffness and associated numerical singularities when $s = 1$.

$$g(s) = (1-k)(1-s)^{m+1} + k \overset{m=1}{\Longrightarrow} g(s) = (1-k)(1-s)^2 + k \tag{25}$$

3.3. Variational energy functional with hydro-mechanical coupling

We consider a domain $\Omega \subset \mathbb{R}^d$ ($d \in \{1, 2, 3\}$) subjected to hydro-mechanical coupling processes, as illustrated in Fig. 2. The external boundary $\partial\Omega$ is partitioned into complementary subsets: $\partial\Omega_u \subset \partial\Omega$ prescribing displacement $\boldsymbol{u}(\boldsymbol{x}, t) \in \mathbb{R}^d$ through time-dependent Dirichlet boundary conditions, and $\partial\Omega_{t^*} \subset \partial\Omega$ specifying traction $\boldsymbol{t}^*(\boldsymbol{x}, t)$ via time-dependent Neumann conditions, where $\boldsymbol{x}$ denotes spatial coordinates and t represents time. The domain Ω is subjected to a body force $\mathbf{b}(\mathbf{x}, t) \in \mathbb{R}^d$, and the internal fracture surface is designated Γ with outward unit normal $\boldsymbol{n}$.

The variational approach to fracture mechanics [32] provides the theoretical foundation. Following established variational formulations for hydraulic fracturing phenomena [52,53], the total energy functional comprises elastic strain energy $\Psi_e(\boldsymbol{\varepsilon})$, fracture

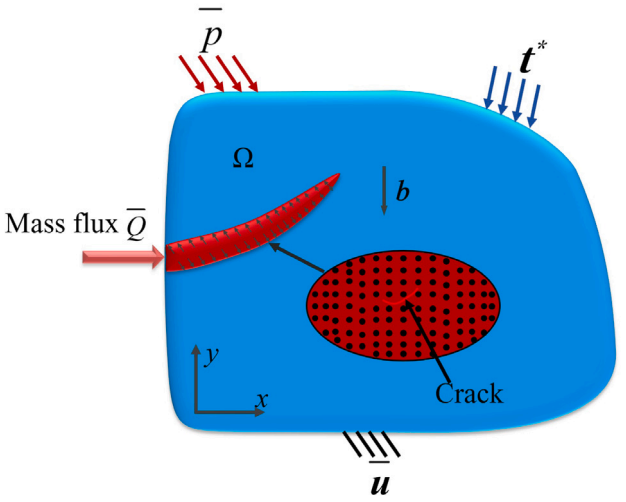

Fig. 2. Schematics of the hydro-mechanical coupling analysis.

energy Ψ_f, external work W_{ext}, body work W_{body}, and the energy contribution from fluid pressure:

$$\begin{aligned}\Pi_\ell(\boldsymbol{u},p,\Gamma) = &\underbrace{\int_{\Omega\setminus\Gamma}\psi_e(\boldsymbol{\varepsilon})\,dV}_{\text{elastic strain energy}} + \underbrace{\int_{\Omega\setminus\Gamma}\boldsymbol{\sigma}^0:\boldsymbol{\varepsilon}\,dV}_{\text{initial stress induced}} - \underbrace{\int_\Omega \alpha p\cdot(\nabla\cdot\boldsymbol{u})\,dV}_{\text{fluid pressure induced}}\\ &+ \underbrace{\int_\Gamma G_c\,d\Gamma}_{\text{fracture energy}} - \underbrace{\int_{\partial\Omega_{t^*}}\boldsymbol{t}^*\cdot\boldsymbol{u}\,dA}_{\text{external work}} - \underbrace{\int_\Omega \boldsymbol{b}\cdot\boldsymbol{u}dV}_{\text{body work}}\end{aligned} \tag{26}$$

where $\boldsymbol{u}$ represents the displacement vector, $\boldsymbol{\sigma}^0$ is initial stress, p denotes pore pressure, α signifies the Biot coefficient, G_c designates the critical fracture energy release rate, $\boldsymbol{t}^*$ the surface traction force, and $\boldsymbol{b}$ the body force density.

The initial stress contribution similarly undergoes degradation through fracture evolution, with its influence diminishing toward zero in the fully fractured domain. Accordingly, we introduce identical degradation for the residual stress work term in Eq. (26) [53]:

$$\int_{\Omega\setminus\Gamma}\boldsymbol{\sigma}^0:\boldsymbol{\varepsilon}\,dV \approx \int_\Omega g(s)\boldsymbol{\sigma}^0:\boldsymbol{\varepsilon}\,dV \tag{27}$$

Incorporating the degraded fracture energy, degraded elastic energy Eq. (24), and modified initial stress term Eq. (27) into Eq. (26), we obtain the complete degraded energy functional:

$$\begin{aligned}\Pi_\ell(\boldsymbol{u},s,p) = &\int_\Omega\left[g(s)\psi_e^+(\boldsymbol{\varepsilon})+\psi_e^-(\boldsymbol{\varepsilon})\right]dV + \int_\Omega g(s)\boldsymbol{\sigma}^0:\boldsymbol{\varepsilon}\,dV\\ &- \int_\Omega \alpha p\cdot(\nabla\cdot\boldsymbol{u})\,dV + \int_\Omega\frac{\Gamma(s)G_c}{\ell}dV - \int_{\partial\Omega_{t^*}}\boldsymbol{t}^*\cdot\boldsymbol{u}\,dA - \int_\Omega\boldsymbol{b}\cdot\boldsymbol{u}dV\end{aligned} \tag{28}$$

3.4. Governing equations for the displacement and damage field

The derivation of the governing equations for hydraulic fracturing employs the variational framework established by Francfort and Marigo [32]. Within this framework, the complete spectrum of fracture phenomena – encompassing nucleation, advancement, bifurcation, and coalescence – emerges naturally through minimization of the total energy functional. The requisite governing relations are derived by computing the first variation of this functional and imposing stationarity conditions, which yields

$$\begin{aligned}\delta\Pi_\ell(\boldsymbol{u},s,p) = &\underbrace{\int_{\partial\Omega_{t^*}}[(\sigma_{ij}^e+g(s)\sigma_{ij}^0-\alpha p\delta_{ij})n_j - t_i^*]\delta u_i\,dA}_{①} - \underbrace{\int_\Omega[(\sigma_{ij}^e+g(s)\sigma_{ij}^0-\alpha p\delta_{ij})_{,j}+b_i]\delta u_i\,dV}_{②}\\ &\underbrace{-\int_\Omega\left[2(1-s)(1-k)(\psi_e^+ + \sigma_{ij}^0\varepsilon_{ij}) - \frac{2G_c s}{\ell}\right]\delta s\,dV}_{③}\\ &\underbrace{+\int_{\partial\Omega}\left(\frac{\partial s}{\partial x_i}n_i\right)\delta s\,dA}_{④} = 0\end{aligned} \tag{29}$$

where n_j denotes the outward normal vector component of the boundary, and σ_{ij}^e refers to a component of the effective trial stress tensor $\boldsymbol{\sigma}^e(\boldsymbol{\varepsilon})$ accounting for degradation, which takes the form

$$\boldsymbol{\sigma}^e(\boldsymbol{\varepsilon}) = [(1-k)(1-s)^2 + k][\lambda\langle \mathrm{tr}(\boldsymbol{\varepsilon})\rangle^+ \mathbf{I} + 2\mu\boldsymbol{\varepsilon}^+] + [\lambda\langle \mathrm{tr}(\boldsymbol{\varepsilon})\rangle^- \mathbf{I} + 2\mu\boldsymbol{\varepsilon}^-] \tag{30}$$

The Cauchy stress tensor is introduced as

$$\boldsymbol{\sigma}^{por}(\boldsymbol{\varepsilon}) = \boldsymbol{\sigma}^e(\boldsymbol{\varepsilon}) + g(s)\boldsymbol{\sigma}^0 - \alpha p \boldsymbol{I} \tag{31}$$

Consequently, the expressions $\sigma_{ij}^e + g(s)\sigma_{ij}^0 - \alpha p\delta_{ij}$ appearing in the boundary integral ① and its spatial derivative $(\sigma_{ij}^e + g(s)\sigma_{ij}^0 - \alpha p\delta_{ij})_{,j}$ in the domain integral ② collectively constitute the poroelastic total stress and its divergence, respectively.

By the fundamental lemma of calculus of variations, the stationarity condition of the Lagrangian energy functional $\delta L(\boldsymbol{u}, s, p) = \delta[\frac{1}{2}\int_\Omega \rho\dot{\boldsymbol{u}}\cdot\dot{\boldsymbol{u}}\mathrm{d}\Omega - \Pi_\ell(\boldsymbol{u}, s, p)] = 0$ must hold for arbitrary variations δu_i and δs, Eq. (29) ② and ③ yield the governing equations

$$\begin{cases} \frac{\partial \sigma_{ij}^{por}}{\partial x_j} + b_i = \rho\ddot{u}_i & \text{in } \Omega \\ s(x_i) = \frac{1}{1+G_c/[\ell(1-k)(\psi_e^+ + \sigma_{ij}^0\varepsilon_{ij})]} & \text{in } \Omega \end{cases} \tag{32}$$

with the boundary conditions from Eq. (29) ① and ④

$$\begin{cases} \boldsymbol{u}_i = \bar{\boldsymbol{u}}_i, & \text{on } \partial\Omega_u \\ \sigma_{ij}^{por} n_j = t_i^*, & \text{on } \partial\Omega_{t^*} \\ \frac{\partial s}{\partial x_i} n_i = 0. & \text{on } \partial\Omega \end{cases} \tag{33}$$

Remark 2 (*On the Boundary Term* ④)**.** It should be noted that the boundary integral ④ in Eq. (29) and the associated natural boundary condition $\frac{\partial s}{\partial x_i} n_i = 0$ arise from integration by parts of a gradient term $|\nabla s|^2$ in the crack surface density function. In the present gradient-free variational damage formulation (Eq. (20)), where the crack density depends only on s and not on ∇s, this boundary term vanishes identically and the condition is trivially satisfied. The term is retained here for generality and to facilitate comparison with classical phase-field formulations that include the gradient regularization.

To enforce the thermodynamically consistent irreversibility constraint wherein fracture cannot heal upon unloading, we introduce a history field $\mathscr{H}$ that tracks the maximum driving force experienced throughout the loading history [53]:

$$\mathscr{H}(\boldsymbol{x}, t) = \max_{\tau\in[0,t]} \left[\psi_e^+(\boldsymbol{\varepsilon}(\boldsymbol{x}, \tau)) + \boldsymbol{\sigma}^0 : \boldsymbol{\varepsilon}(\boldsymbol{x}, \tau)\right] \tag{34}$$

Substituting this history variable for the instantaneous driving force in Eq. (32) yields the final form of governing equations:

$$\begin{cases} \frac{\partial \sigma_{ij}^{por}}{\partial x_j} + b_i = \rho\ddot{u}_i & \text{in } \Omega \\ s(x_i) = \frac{1}{1+G_c/[\ell(1-k)\mathscr{H}]} & \text{in } \Omega \end{cases} \tag{35}$$

3.5. Governing equations of the flow field

Fluid transport within the porous medium Ω is governed by Darcy's law. The computational domain is partitioned into three distinct regions: Ω_r denoting the intact reservoir domain, Ω_f representing the fracture domain, and Ω_t characterizing the intermediate transition domain. Following the methodology of Lee et al. [52], the damage field variable s serves as the discriminator for domain classification through two critical thresholds c_1 and c_2. Specifically, regions satisfying $s \le c_1$ are identified as reservoir domains, whereas those meeting $s \ge c_2$ constitute fracture domains, with $c_1 < s < c_2$ defining the transitional zones. The fracture, reservoir and transition domains are illustrated in Fig. 3.

In the reservoir domain Ω_r, the governing equations for mass balance in the poroelastic continuum are formulated as

$$\rho_r \mathbb{s}_r \frac{\partial p}{\partial t} + \nabla\cdot(\rho_r \mathbf{v}_r) = Q_r - \rho_r \alpha_r \frac{\partial \varepsilon_{vol}}{\partial t} \tag{36}$$

where ρ_r denotes fluid density, $\mathbb{s}_r$ represents storage coefficient, $\mathbf{v}_r$ signifies the Darcy velocity vector, Q_r represents a fluid source term, and $\varepsilon_{vol} = \nabla\cdot\boldsymbol{u}$ designates volumetric strain.

The flow velocity $\mathbf{v}_r$ is related to the pressure gradient ∇p by Darcy's law:

$$\mathbf{v}_r = -\frac{K_r}{\mu_r}(\nabla p + \rho_r \mathbf{g}) \tag{37}$$

where K_r represents the reservoir permeability, μ_r denotes the fluid dynamic viscosity, and $\mathbf{g}$ signifies the gravity vector.

The storage coefficient $\mathbb{s}_r$, which characterizes the compressibility response of a porous medium, is defined as a function of the material porosity $\mathbb{n}_r$. According to [29], it can be expressed as:

$$\mathbb{s}_r = \frac{(\alpha_r - \mathbb{n}_r)(1-\alpha_r)}{\mathbb{k}_r} + \frac{\mathbb{n}_r}{\mathbb{k}_w} \tag{38}$$

where $\mathbb{k}_r$, $\mathbb{k}_w$ denote the bulk modulus of the media and fluid, respectively.

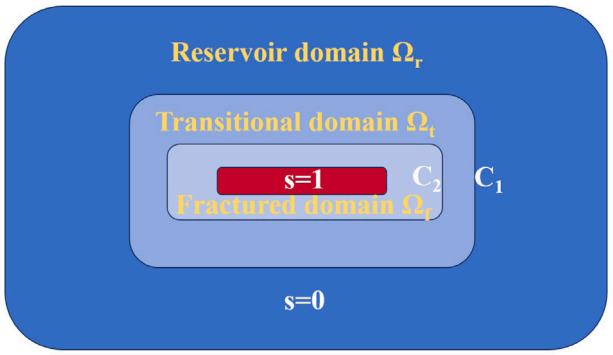

Fig. 3. The fracture, reservoir and transition domains.

Substituting Eq. (37) into Eq. (36), the governing diffusion equation for the fluid field takes the form

$$\nabla \cdot \frac{\rho_r K_r}{\mu_r}(\nabla p + \rho_r \mathbf{g}) + Q_r = \rho_r \mathbb{s}_r \frac{\partial p}{\partial t} + \rho_r \alpha_r \frac{\partial \varepsilon_{vol}}{\partial t} \tag{39}$$

In the fracture domain Ω_f, the bulk strain rate can be considered negligible, and consequently the governing equation for fluid diffusion in the fracture domain reduces to

$$\nabla \cdot \frac{\rho_f K_f}{\mu_f}(\nabla p + \rho_f \mathbf{g}) + Q_f = \rho_f \mathbb{s}_f \frac{\partial p}{\partial t} \tag{40}$$

where $\mathbb{s}_f$, K_f, Q_f, μ_f, and ρ_f are the storage coefficient, permeability, source term, fluid viscosity, and fluid density in the fracture domain.

The validity of the cubic law formulation requires satisfaction of specific flow regime constraints, as demonstrated in prior investigations [5]. For plane flow problems, the fracture permeability can be expressed as:

$$K_f = \frac{w^2}{12} \tag{41}$$

where the aperture w denotes the hydraulic aperture.

The hydraulic aperture w at each material point in the damaged zone is computed following a bond-level decomposition strategy adapted from Ni et al. [29]. For a material point i identified as belonging to the fracture domain ($s \geq c_2$), we consider all neighboring material points j within its horizon whose connecting bonds cross the fracture surface. For each such bond $\boldsymbol{\xi}_{ij}$, the relative displacement vector $\boldsymbol{\eta}_{ij} = \mathbf{u}_j - \mathbf{u}_i$ is decomposed into components along and perpendicular to the original bond direction. The perpendicular component represents the crack opening displacement, while the parallel component corresponds to the shear dislocation. Accordingly, the aperture contribution from bond $\boldsymbol{\xi}_{ij}$ is expressed as:

$$a_{ij} = \|\boldsymbol{\xi}_{ij}\|^d \cos\beta_{ij} - \|\boldsymbol{\xi}_{ij}\|^o \tag{42a}$$

where $\|\boldsymbol{\xi}_{ij}\|^o$ and $\|\boldsymbol{\xi}_{ij}\|^d$ denote the original and deformed bond lengths, respectively, and β_{ij} is the angle between the initial and deformed bond directions. This decomposition extracts the normal opening component of the bond deformation and filters out the tangential sliding contribution, thereby avoiding spurious permeability updates at closed cracks undergoing shear dislocation. The aperture at material point i is then obtained by averaging over all qualifying bonds:

$$w_i = \frac{1}{n}\sum a_{ij} \tag{42b}$$

where n is the number of bonds satisfying both $a_{ij} \geq 0$ (indicating opening rather than closure) and the damage criterion at the bond endpoints. Only bonds with non-negative opening contributions are included, ensuring that the computed aperture reflects the actual fracture width. The resulting aperture w_i is substituted into Eq. (41) to update the fracture permeability at each damaged material point.

To establish continuity between the reservoir and fracture domains, transition functions are introduced following the methodology of [52,54]. Two piecewise-linear indicator functions, $\chi_r(\mathbf{x}, t, s)$ (hereafter abbreviated as χ_r) and $\chi_f(\mathbf{x}, t, s)$ (abbreviated as χ_f), are formulated as functions of the damage field to characterize the material state across these domains, as illustrated in Fig. 4. These functions satisfy the following constraints:

$$\begin{cases} \chi_r(\mathbf{x}, t, s) = 1 & \text{in } \Omega_r \\ \chi_r(\mathbf{x}, t, s) = 0 & \text{in } \Omega_f \\ \chi_f(\mathbf{x}, t, s) = 1 & \text{in } \Omega_f \\ \chi_f(\mathbf{x}, t, s) = 0 & \text{in } \Omega_r \end{cases} \tag{43}$$

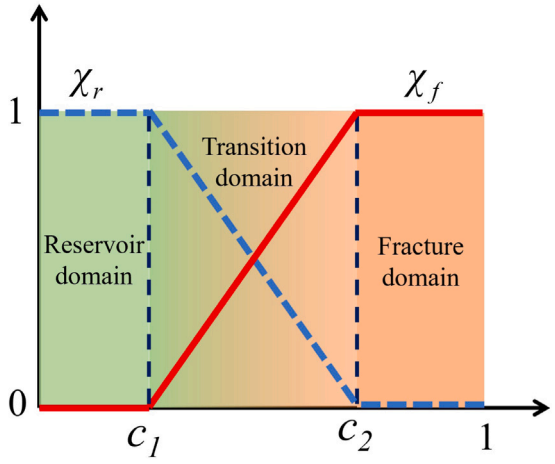

Fig. 4. Linear indicator functions χ_r and χ_f.

Within the transition region Ω_t, these indicator functions are expressed through linear relationships with the damage parameter:

$$\chi_r(\mathbf{x},t,s)=\frac{c_2-s}{c_2-c_1},\quad \chi_f(\mathbf{x},t,s)=\frac{s-c_1}{c_2-c_1} \tag{44}$$

Material and transport properties within Ω_t are determined through weighted interpolation between the corresponding reservoir and fracture properties using these indicator functions. Specifically, the effective fluid density, Biot coefficient, dynamic viscosity, permeability, and storage coefficient are computed as:

$$\begin{cases}\rho_t=\rho_r\chi_r+\rho_f\chi_f,\\ \alpha_t=\alpha_r\chi_r+\alpha_f\chi_f,\\ \mu_t=\mu_r\chi_r+\mu_f\chi_f,\\ K_t=K_r\chi_r+K_f\chi_f,\\ \mathbb{s}_t=\mathbb{s}_r\chi_r+\mathbb{s}_f\chi_f.\end{cases} \tag{45}$$

Employing these interpolated properties, the mass conservation equation governing fluid transport in the transition domain is formulated as:

$$\nabla\cdot\frac{\rho_t K_t}{\mu_t}(\nabla p+\rho_t\mathbf{g})+Q_t=\rho_t\mathbb{s}_t\frac{\partial p}{\partial t}+\rho_t\alpha_t\frac{\partial\varepsilon_{vol}}{\partial t} \tag{46}$$

where $\mathbb{s}_t$, K_t, Q_t, μ_t, α_t, and ρ_t represent the effective storage coefficient, permeability, volumetric source term, fluid viscosity, Biot coefficient, and fluid density, respectively, evaluated within the transition domain.

The fluid field is subject to boundary conditions wherein Dirichlet-type constraints are imposed on $\partial\Omega_d$ while Neumann-type constraints are enforced on $\partial\Omega_n$, where these boundary segments satisfy the disjoint condition $\partial\Omega_d\cap\partial\Omega_n=\emptyset$:

$$\begin{cases}p=\bar{p}, & \text{on } \partial\Omega_d\\ -\boldsymbol{n}\cdot\rho\mathbf{v}_r=\bar{Q}. & \text{on } \partial\Omega_n\end{cases} \tag{47}$$

where $\bar{p}$ prescribes fluid pressure along the Dirichlet boundary segment and $\bar{Q}$ specifies the mass flux applied at the Neumann boundary portion.

The complete governing system for damage modeling of hydraulic fracture propagation comprises the coupled mechanical equilibrium, damage field evolution, and mass conservation:

$$\frac{\partial\sigma_{ij}^{por}}{\partial x_j}+b_i=\rho\ddot{u}_i \qquad \text{in } \Omega \tag{48a}$$

$$s(x_i)=\frac{1}{1+G_c/[\ell(1-k)\mathscr{H}]} \qquad \text{in } \Omega \tag{48b}$$

$$\nabla\cdot\left[\frac{\rho_r K_r}{\mu_r}(\nabla p+\rho_r\mathbf{g})\right]+Q_r=\rho_r\mathbb{s}_r\frac{\partial p}{\partial t}+\rho_r\alpha_r\frac{\partial\varepsilon_{vol}}{\partial t} \qquad \text{in } \Omega_r \tag{48c}$$

$$\nabla\cdot\left[\frac{\rho_f K_f}{\mu_f}(\nabla p+\rho_f\mathbf{g})\right]+Q_f=\rho_f\mathbb{s}_f\frac{\partial p}{\partial t} \qquad \text{in } \Omega_f \tag{48d}$$

$$\nabla\cdot\left[\frac{\rho_t K_t}{\mu_t}(\nabla p+\rho_t\mathbf{g})\right]+Q_t=\rho_t\mathbb{s}_t\frac{\partial p}{\partial t}+\rho_t\alpha_t\frac{\partial\varepsilon_{vol}}{\partial t} \qquad \text{in } \Omega_t \tag{48e}$$

with the boundary conditions

$$\begin{cases} \boldsymbol{u}_i = \bar{\boldsymbol{u}}_i, & \text{on } \partial\Omega_u \\ \sigma_{ij}^{por} n_j = t_i^*, & \text{on } \partial\Omega_{t^*} \\ \frac{\partial s}{\partial x_i} n_i = 0, & \text{on } \partial\Omega \\ p = \bar{p}, & \text{on } \partial\Omega_d \\ -\boldsymbol{n} \cdot \rho_f \mathbf{v}_f = \bar{Q}. & \text{on } \partial\Omega_n \end{cases} \tag{49}$$

The solution of this coupled system Eqs. (48) and (49) yields the complete spatiotemporal evolution of displacement $\boldsymbol{u}(\boldsymbol{x}, t)$, damage field $s(\boldsymbol{x}, t)$, and pressure $p(\boldsymbol{x}, t)$ fields.

3.6. Governing equations for hydro-mechanical VDM in DH-NOSBPD

The integration of the hydro-mechanical variational damage model within the DH-NOSBPD framework requires careful treatment of both the nonlocal mechanical interactions and the flow field evolution. The coupled hydro-mechanical system requires simultaneous solution of displacement and flow fields. According to Eq. (12), the governing equation for material point $\boldsymbol{x}_i$ becomes

$$\int_{\mathcal{H}_i} (\omega(\boldsymbol{\xi}_{ij}) \boldsymbol{\sigma}_i^{por} \boldsymbol{K}_i^{-1} \boldsymbol{\xi}_{ij} + \boldsymbol{\mathcal{F}}_{ij}^{\boldsymbol{u}}) dV_j - \int_{\mathcal{H}_i'} (\omega(\boldsymbol{\xi}_{ji}) \boldsymbol{\sigma}_j^{por} \boldsymbol{K}_j^{-1} \boldsymbol{\xi}_{ji} + \boldsymbol{\mathcal{F}}_{ji}^{\boldsymbol{u}}) dV_j + \boldsymbol{b}_i = \rho_i \ddot{\boldsymbol{u}}_i \tag{50}$$

$$\begin{aligned} &\int_{\mathcal{H}_i} (\omega(\boldsymbol{\xi}_{ij}) \frac{\rho_i K_i}{\mu_i} (\tilde{\nabla} p_i + \rho_i \mathbf{g}_i) \boldsymbol{K}_i^{-1} \boldsymbol{\xi}_{ij} + \boldsymbol{\mathcal{F}}_{ij}^{p}) dV_j \\ &- \int_{\mathcal{H}_i'} (\omega(\boldsymbol{\xi}_{ji}) \frac{\rho_j K_j}{\mu_j} (\tilde{\nabla} p_j + \rho_j \mathbf{g}_j) \boldsymbol{K}_j^{-1} \boldsymbol{\xi}_{ji} + \boldsymbol{\mathcal{F}}_{ji}^{p}) dV_j + Q_i = \rho_i \mathbb{s}_i \dot{p}_i + \rho_i \alpha_i \dot{\varepsilon}_{voli} \end{aligned} \tag{51}$$

where the Cauchy stress tensor at each material point incorporates flow field effects:

$$\begin{cases} \boldsymbol{\sigma}_i^{por} = \frac{\boldsymbol{\sigma}_i^+(\boldsymbol{\varepsilon}_i^e) + \boldsymbol{\sigma}_i^0}{\{1 + [\ell(1-k)\mathscr{H}]/G_c\}^2} + \boldsymbol{\sigma}_i^-(\boldsymbol{\varepsilon}_i^e) - \alpha p_i \boldsymbol{I} \\ \boldsymbol{\sigma}_j^{por} = \frac{\boldsymbol{\sigma}_j^+(\boldsymbol{\varepsilon}_j^e) + \boldsymbol{\sigma}_j^0}{\{1 + [\ell(1-k)\mathscr{H}]/G_c\}^2} + \boldsymbol{\sigma}_j^-(\boldsymbol{\varepsilon}_j^e) - \alpha p_j \boldsymbol{I} \end{cases} \tag{52}$$

To account for fracture discontinuity in the model, a degradation mechanism is applied to the stabilization force. This is achieved through the incorporation of a damage coefficient, expressed as $1/\{1+[\ell(1-k)\mathscr{H}]/G_c\}$, which modifies the terms $\boldsymbol{\mathcal{F}}_{ij}^{hg}(\boldsymbol{u})$ and $\boldsymbol{\mathcal{F}}_{ij}^{hg}(p)$. Consequently, the resulting stabilization force for the hourglass mode incorporates the influence of damage evolution as follows:

$$\boldsymbol{\mathcal{F}}_{ij}^{\boldsymbol{u}} = \frac{\boldsymbol{\mathcal{F}}_{ij}^{hg}(\boldsymbol{u})}{1 + [\ell(1-k)\mathscr{H}]/G_c} = \frac{1}{1 + [\ell(1-k)\mathscr{H}]/G_c} \frac{2p_{hg}}{m_{\boldsymbol{K}_i}} \omega(\boldsymbol{\xi}_{ij})(\boldsymbol{u}_{ij} - \tilde{\nabla}\boldsymbol{u}_i \cdot \boldsymbol{\xi}_{ij}) \tag{53}$$

$$\boldsymbol{\mathcal{F}}_{ij}^{p} = \frac{\boldsymbol{\mathcal{F}}_{ij}^{hg}(p)}{1 + [\ell(1-k)\mathscr{H}]/G_c} = \frac{1}{1 + [\ell(1-k)\mathscr{H}]/G_c} \frac{2p_{hg}}{m_{\boldsymbol{K}_i}} \omega(\boldsymbol{\xi}_{ij})(p_{ij} - \tilde{\nabla} p_i \cdot \boldsymbol{\xi}_{ij}). \tag{54}$$

4. Numerical implementation

The numerical realization of the coupled hydro-mechanical variational damage model within the DH-NOSBPD framework is described in this section. The discussion covers spatial discretization, temporal advancement schemes, the partitioned solution algorithm, and quasi-static analysis via adaptive dynamic relaxation. Detailed algorithmic pseudocodes are included to facilitate practical implementation.

4.1. Spatial discretization

The spatial domain Ω is discretized into N material points $\{\mathbf{x}_i\}_{i=1}^N$, each occupying a volume V_i (as shown in Fig. 5). For regular grid discretizations with uniform spacing Δx, the volume is $V_i = (\Delta x)^d$.

Non-uniform discretization can be achieved through adaptive refinement, with local grid spacing varying to concentrate resolution in regions of interest. The dual-horizon framework naturally accommodates such non-uniform discretization. For each material point i, the horizon domain in discrete form can be denoted by a list of neighbors:

$$\mathcal{H}_i = \{i, j_1, j_2, \ldots, j_{n_i}\} \tag{55}$$

where n_i is the number of neighbors in the horizon domain of point i.

In discrete form, the shape tensor and nonlocal gradient operator at particle i become

$$\boldsymbol{K}_i = \sum_{j \in \mathcal{H}_i} \omega(\boldsymbol{\xi}_{ij}) \boldsymbol{\xi}_{ij} \otimes \boldsymbol{\xi}_{ij} \Delta V_j \tag{56}$$

$$\tilde{\nabla}\boldsymbol{u}_i = \sum_{j \in \mathcal{H}_i} \omega_{ij}(\boldsymbol{u}_j - \boldsymbol{u}_i) \otimes \boldsymbol{\xi}_{ij} \Delta V_j \cdot \boldsymbol{K}_i^{-1} \tag{57}$$

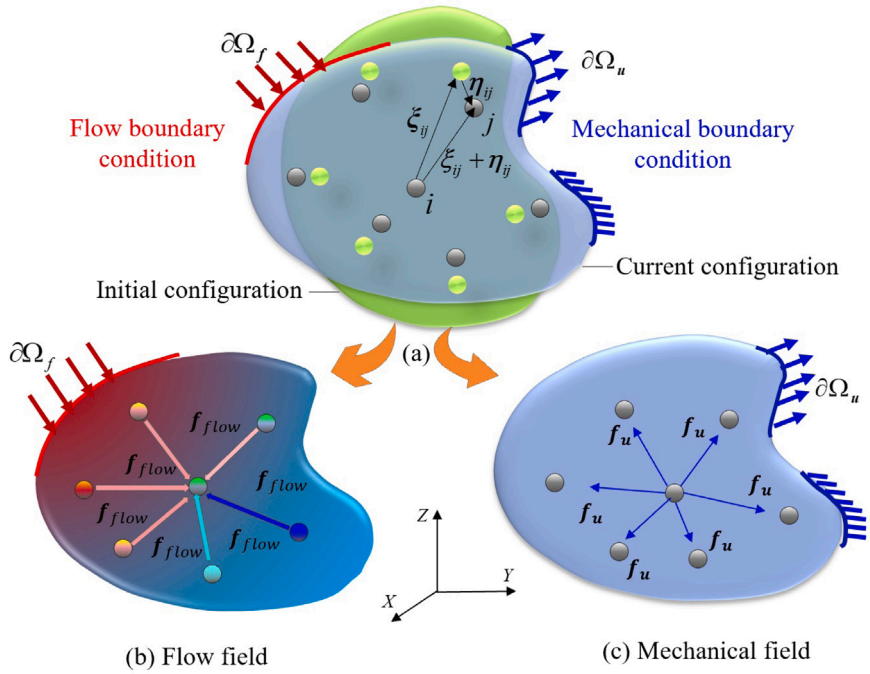

Fig. 5. The spatial discretization in flow and mechanical fields.

The discrete forms of Eqs. (50) and (51) read

$$\sum_{j\in\mathcal{H}_i}(\omega(\boldsymbol{\xi}_{ij})\boldsymbol{\sigma}_i^{por}\boldsymbol{K}_i^{-1}\boldsymbol{\xi}_{ij}+\boldsymbol{\mathcal{F}}_{ij}^{\boldsymbol{u}})\Delta V_j-\sum_{j\in\mathcal{H}_i'}(\omega(\boldsymbol{\xi}_{ji})\boldsymbol{\sigma}_j^{por}\boldsymbol{K}_j^{-1}\boldsymbol{\xi}_{ji}+\boldsymbol{\mathcal{F}}_{ji}^{\boldsymbol{u}})\Delta V_j+\boldsymbol{b}_i=\rho_i\ddot{\boldsymbol{u}}_i \tag{58}$$

$$\sum_{j\in\mathcal{H}_i}(\omega(\boldsymbol{\xi}_{ij})\frac{\rho_i K_i}{\mu_i}(\tilde{\nabla}p_i+\rho_i\mathbf{g}_i)\boldsymbol{K}_i^{-1}\boldsymbol{\xi}_{ij}+\boldsymbol{\mathcal{F}}_{ij}^{p})\Delta V_j$$
$$-\sum_{j\in\mathcal{H}_i'}(\omega(\boldsymbol{\xi}_{ji})\frac{\rho_j K_j}{\mu_j}(\tilde{\nabla}p_j+\rho_j\mathbf{g}_j)\boldsymbol{K}_j^{-1}\boldsymbol{\xi}_{ji}+\boldsymbol{\mathcal{F}}_{ji}^{p})\Delta V_j+Q_i=\rho_i\mathbb{s}_i\dot{p}_i+\rho_i\alpha_i\dot{\varepsilon}_{voli} \tag{59}$$

4.2. Temporal integration schemes

The mechanical governing equation Eq. (58) represents a second-order system of ordinary differential equations in time. For explicit time integration, the velocity-Verlet algorithm [55] provides second-order accuracy and good stability properties:

Algorithm 1 Velocity-Verlet Time Integration

1: **Input:** $\mathbf{u}_i^n$, $\mathbf{v}_i^n$ for all i, Time step Δt
2: **Output:** $\mathbf{u}_i^{n+1}$, $\mathbf{v}_i^{n+1}$
3: Compute forces: $\mathbf{F}_i^n$ from Eq. (58)
4: Compute acceleration: $\mathbf{a}_i^n=\mathbf{F}_i^n/\rho$
5: Update velocity (half-step): $\mathbf{v}_i^{n+1/2}=\mathbf{v}_i^n+\frac{\Delta t}{2}\mathbf{a}_i^n$
6: Update displacement: $\mathbf{u}_i^{n+1}=\mathbf{u}_i^n+\Delta t\mathbf{v}_i^{n+1/2}$
7: Compute acceleration at new time: $\mathbf{a}_i^{n+1}=\mathbf{F}_i^{n+1}/\rho$
8: Update velocity (full-step): $\mathbf{v}_i^{n+1}=\mathbf{v}_i^{n+1/2}+\frac{\Delta t}{2}\mathbf{a}_i^{n+1}$

The explicit time integration requires a time step satisfying the CFL stability condition [56]. For peridynamic simulations, the critical time step is approximately

$$\Delta t_{crit}\approx\sqrt{\frac{\rho\Delta x_{\min}^2}{(\lambda_{\max}+2\mu_{\max})}} \tag{60}$$

where $\Delta x_{\min}$ is the minimum particle spacing. For numerical stability, the actual time step is taken as:

$$\Delta t=0.7\Delta t_{crit} \tag{61}$$

The pore pressure diffusion equation Eq. (59) is a first-order system in time. Forward Euler integration provides a simple explicit scheme [57]:

$$p_i^{n+1} = p_i^n + \frac{\Delta t_p}{\mathbb{S}_i}\left[\sum_{j\in\mathcal{H}_i}[\omega(\xi_{ij})\frac{K_i}{\mu_i}(\frac{p_j^n - p_i^n}{\|\xi_{ij}\|^2} + \mathbf{g}_i) + \mathcal{F}_{ij}^p]\Delta V_j - \sum_{j\in\mathcal{H}_i'}[\omega(\xi_{ji})\frac{K_j}{\mu_j}(\frac{p_i^n - p_j^n}{\|\xi_{ji}\|^2} + \mathbf{g}_j) + \mathcal{F}_{ji}^p]\Delta V_j - \alpha_i\frac{\varepsilon_{voli}^{n+1} - \varepsilon_{voli}^n}{\Delta t_p} + \frac{Q_i}{\rho_i}\right] \tag{62}$$

The diffusion process imposes a stability constraint on the pressure time step:

$$\Delta t_p = \alpha_{\text{safe}}\frac{\mu\mathbb{S}\Delta x_{\min}^2}{4K_{max}} \tag{63}$$

where K_{max} is the maximum permeability in the system, and $\alpha_{\text{safe}} \in [0.7, 0.9]$ is a safety factor.

Remark 3 (*Explicit Versus Implicit/semi-Implicit Coupling for Stiff Problems*)**.** The explicit coupling scheme adopted in this work offers computational simplicity and parallelization efficiency, but may encounter stability limitations when addressing stiff hydro-mechanical problems characterized by large permeability contrasts (e.g., $K_f/K_r > 10^4$) or rapid pressure transients near propagating fracture tips. In such scenarios, the stability constraint in Eq. (63) can become prohibitively restrictive, as the time step scales inversely with the maximum permeability.

For problems exhibiting pronounced stiffness, implicit or semi-implicit time integration schemes offer potential advantages. A semi-implicit approach, wherein the pressure diffusion equation is treated implicitly while the mechanical equilibrium remains explicit, can substantially relax the stability constraint associated with fluid transport while preserving the computational efficiency of explicit mechanical integration. Fully implicit monolithic schemes, though computationally more demanding due to the necessity of assembling and solving coupled linear systems, provide unconditional stability and enable arbitrarily large time steps constrained only by accuracy requirements.

The present explicit formulation remains well-suited for the class of problems investigated herein, where permeability contrasts are moderate and the adaptive time stepping strategy adequately captures the relevant physics. Nevertheless, extension to implicit or semi-implicit formulations represents a natural avenue for future development, particularly for applications involving extreme permeability heterogeneity or very rapid injection scenarios where explicit methods become computationally inefficient.

4.3. Adaptive dynamic relaxation

For quasi-static problems where inertial effects are negligible, the explicit dynamic integration converges slowly to equilibrium. Adaptive Dynamic Relaxation (ADR) provides an efficient alternative by introducing artificial damping that accelerates convergence to steady state. This numerical scheme augments the governing equation of motion with a viscous damping term that is proportional to the nodal velocity:

$$\rho\ddot{\mathbf{u}}_i + c_i\dot{\mathbf{u}}_i = \mathbf{F}_i \tag{64}$$

where c_i denotes the damping coefficient associated with material point i, and $\mathbf{F}_i$ represents the resultant force vector computed from Eq. (58).

A distinguishing characteristic of the ADR scheme lies in its capability to dynamically calibrate the damping parameters throughout the iterative process, thereby accelerating the convergence toward static equilibrium. For material point i at the nth time step, the critically damped condition yields the optimal damping coefficient as:

$$c_i^n = 2\sqrt{\rho K_i^n} \tag{65}$$

in which K_i^n represents a local estimate of the material stiffness.

The local stiffness is evaluated based on incremental force–displacement relationships. To ensure numerical robustness, a regularization procedure is introduced:

$$K_i^n = \begin{cases} \frac{\|\mathbf{F}_i^n - \mathbf{F}_i^{n-1}\|}{\|\mathbf{u}_i^n - \mathbf{u}_i^{n-1}\|} & \text{if } \|\mathbf{u}_i^n - \mathbf{u}_i^{n-1}\| > \epsilon_u \\ K_i^{n-1} & \text{otherwise} \end{cases} \tag{66}$$

where ϵ_u serves as a numerical tolerance parameter (typically set to 10^{-10} in normalized units) that prevents potential numerical instabilities arising from vanishing displacement increments.

Remark 4 (*Regularization and Filtering for Local Stiffness Estimation*)**.** The local stiffness estimate defined in Eq. (66) may exhibit sensitivity to numerical noise, particularly in regions undergoing rapid damage evolution, near material interfaces, or where

displacement increments approach machine precision. Such noise sensitivity can manifest as spurious oscillations in the damping coefficient, potentially compromising convergence behavior or inducing localized numerical instabilities.

To enhance robustness against noise contamination, several regularization and filtering strategies are employed. First, a temporal smoothing filter is applied to the stiffness estimate:

$$\bar{K}_i^n = \beta K_i^n + (1-\beta)\bar{K}_i^{n-1}, \tag{67}$$

where $\beta \in (0,1]$ denotes a smoothing parameter (typically $\beta = 0.3$–0.7) that controls the degree of temporal averaging. This exponential moving average effectively attenuates high-frequency fluctuations while preserving the adaptive character of the scheme.

Second, bounding constraints are imposed to preclude extreme stiffness values:

$$K_i^n \leftarrow \max\left(K_{\min}, \min\left(K_i^n, K_{\max}\right)\right), \tag{68}$$

where $K_{\min}$ and $K_{\max}$ are problem-dependent bounds, typically estimated from the elastic moduli and characteristic length scales (e.g., $K_{\min} = 0.01E/\Delta x$ and $K_{\max} = 100E/\Delta x$).

Third, spatial smoothing through neighborhood averaging can mitigate localized noise artifacts:

$$\bar{K}_i^n = \frac{\sum_{j\in\mathcal{H}_i} \omega(\boldsymbol{\xi}_{ij}) K_j^n \Delta V_j}{\sum_{j\in\mathcal{H}_i} \omega(\boldsymbol{\xi}_{ij}) \Delta V_j}. \tag{69}$$

In the present implementation, the threshold-based regularization in Eq. (66), combined with temporal smoothing (Eq. (67) with $\beta = 0.5$), has proven sufficient for all numerical examples considered herein. For problems exhibiting more pronounced noise characteristics, the supplementary filtering techniques described above may be activated as needed.

The computational procedure for implementing the ADR method is presented in Algorithm 2. The scheme employs a predictor–corrector formulation based on central difference time integration, where velocity and displacement fields are updated in a staggered manner.

Algorithm 2 Adaptive Dynamic Relaxation

Input: Initial configuration $\mathbf{u}_i^0$, target residual R_{tol}
Output: Quasi-static equilibrium configuration $\mathbf{u}_i$
Initialize: $\mathbf{v}_i^0 = \mathbf{0}$, $K_i^0 = K_{init}$
$n \leftarrow 0$
repeat
  Compute forces: $\mathbf{F}_i^n$ from Eq. (58)
  Compute residual: $R^n = \sqrt{\sum_i \|\mathbf{F}_i^n\|^2 / N}$
  if $R^n < R_{tol}$ **then**
    break
  end if
  Update local stiffness: K_i^n using Eq. (66)
  Compute damping: c_i^n using Eq. (65)
  Compute damped acceleration: $\mathbf{a}_i^n = (\mathbf{F}_i^n - c_i^n \mathbf{v}_i^n)/\rho$
  Update velocity: $\mathbf{v}_i^{n+1/2} = \mathbf{v}_i^n + \frac{\Delta t}{2}\mathbf{a}_i^n$
  Update displacement: $\mathbf{u}_i^{n+1} = \mathbf{u}_i^n + \Delta t \mathbf{v}_i^{n+1/2}$
  Compute forces: $\mathbf{F}_i^{n+1}$
  Compute damped acceleration: $\mathbf{a}_i^{n+1} = (\mathbf{F}_i^{n+1} - c_i^n \mathbf{v}_i^{n+1/2})/\rho$
  Update velocity: $\mathbf{v}_i^{n+1} = \mathbf{v}_i^{n+1/2} + \frac{\Delta t}{2}\mathbf{a}_i^{n+1}$
  $n \leftarrow n+1$
until maximum iterations reached

The computational efficiency of the ADR scheme stems from its adaptive damping mechanism, which maintains near-critical damping conditions throughout the solution process.

4.4. Staggered solution algorithm

The coupled hydro-mechanical system is solved using a staggered approach, where hydraulic and mechanical fields are updated sequentially within each time step. The staggered algorithm proceeds as follows for each global time step :

Algorithm 3 Staggered Solution for Coupled Hydro-Mechanical Problem

Input: Material properties, geometry, boundary conditions, final time t_{final}
Output: Displacement field $\mathbf{u}_i$, pressure field p_i, damage field s_i
Initialization:
  Generate material point positions $\{\mathbf{x}_i\}_{i=1}^{N}$
  Construct neighbor lists: $\mathcal{H}_i$, $\mathcal{H}_i'$ for all i
  Compute shape tensor $\mathbf{K}_i^n$ (Eq. (56)), nonlocal gradient $\tilde{\nabla}\boldsymbol{u}_i^n$ (Eq. (57)):
  Compute strain tensor: $\boldsymbol{\varepsilon}_i^n = \frac{1}{2}[\tilde{\nabla}\boldsymbol{u}_i^n + (\tilde{\nabla}\boldsymbol{u}_i^n)^T]$
  Perform spectral decomposition: $\boldsymbol{\varepsilon}_i^n = \sum_{k=1}^{3} \varepsilon_{ik}^n \boldsymbol{n}_{ik} \otimes \boldsymbol{n}_{ik}$
  Compute stress: $\boldsymbol{\sigma}_i^{por}$ (Eqs. (30),(31))
  Initialize fields: $\mathbf{u}_i^0 = \mathbf{0}$, $p_i^0 = p_0$, $s_i^0 = 0$, $\mathscr{H}_i^0 = 0$
$t \leftarrow 0$, $n \leftarrow 0$
while $t < t_{\text{final}}$ **do**
  //**Pressure Update:**
    Compute pressure time step: Δt_p (Eq. (63))
    Update pressure: p_i^{n+1} (Eq. (62))
    Apply pressure boundary conditions

  //**Mechanical Update:**
  if new damage detected or significant load change **then**
      Run ADR to equilibrium (Algorithm 2)
  else
      Single explicit mechanical step (Algorithm 1)
  end if
    Update strain and stress: $\boldsymbol{\epsilon}_i^{n+1}$, $(\boldsymbol{\sigma}_i^{n+1})^{por}$ (Eqs. (30),(31))
  Apply displacement boundary conditions

  //**Damage Update:**
    Compute positive strain energy: $\psi_{ei}^{+}(\boldsymbol{\varepsilon}_i^{n+1}) = \frac{\lambda}{2}\langle \mathrm{tr}(\boldsymbol{\varepsilon}_i^{n+1})\rangle_+^2 + \mu \mathrm{tr}(((\boldsymbol{\varepsilon}_i^{n+1})^+)^2)$ [9]
    Update history variable: $\mathscr{H}_i^{n+1} = \max[\mathscr{H}_i^n, \psi_{ei}^{+}(\boldsymbol{\varepsilon}_i^{n+1}) + \boldsymbol{\sigma}_i^0 : \boldsymbol{\varepsilon}_i^{n+1}]$
    Update damage: s_i^{n+1} (Eq. (48b))

  // **Material and transport properties Update:**
    Update $\mathbb{s}_i^{n+1}$, K_i^{n+1}, Q_i^{n+1}, μ_i^{n+1}, α_i^{n+1}, and ρ_i^{n+1} based on damage s_i^{n+1} (Eqs. (44),(45))

  $t \leftarrow t + \Delta t$, $n \leftarrow n + 1$
end while

The staggered algorithm provides several advantages. First, it decouples the solution of different field equations, enabling use of specialized solvers optimized for each physics. Second, it allows different time step sizes for different fields, accommodating disparate time scales. Third, it reduces memory requirements compared to fully coupled monolithic solvers. However, the staggered approach requires careful selection of time step sizes and convergence tolerances to maintain accuracy of the coupling.

Remark 5 (*Convergence Criteria and Coupling Error Control*)**.** The accuracy of the staggered solution scheme depends critically on appropriate convergence criteria and mechanisms for controlling coupling errors between the mechanical and hydraulic subsystems. Several strategies are employed in the present implementation to ensure solution fidelity.

Mechanical equilibrium convergence. Within each global time step, the ADR solver iterates until the normalized residual force satisfies:

$$R^n = \frac{\sqrt{\sum_i \|\mathbf{F}_i^n\|^2}}{\sqrt{\sum_i \|\mathbf{F}_i^{ext}\|^2} + \epsilon_F} < R_{tol} \tag{70}$$

where $\mathbf{F}_i^{ext}$ represents the external force contribution (including pressure-induced body forces) and ϵ_F is a small regularization parameter to handle cases with vanishing external loads. A typical tolerance of $R_{tol} = 10^{-6}$ to 10^{-8} is employed.

Pressure field convergence. For the explicit pressure update, stability is ensured through the CFL-type constraint in Eq. (63).

Coupling error control. The sequential staggered approach introduces a splitting error of order $\mathcal{O}(\Delta t)$ due to the explicit treatment of inter-field coupling. This error can be controlled through several mechanisms:

(i) *Time step restriction:* The global time step is selected to satisfy both the mechanical and hydraulic stability constraints, with an additional restriction based on the characteristic coupling time scale:

$$\Delta t \leq \min\left(\Delta t_{crit}, \Delta t_p, \frac{\alpha_c \ell^2}{c_v}\right) \tag{71}$$

where $c_v = K/(\mu \mathbb{s})$ is the consolidation coefficient and $\alpha_c \in [0.1, 0.5]$ is a coupling safety factor.

(ii) *Fixed-point iterations:* For strongly coupled problems, sub-iterations between mechanical and hydraulic solvers within each global time step can reduce splitting errors:

$$\text{Iterate: } p^{n+1,(k)} \to \mathbf{u}^{n+1,(k)} \to p^{n+1,(k+1)} \text{ until } \|\mathbf{u}^{n+1,(k+1)} - \mathbf{u}^{n+1,(k)}\| < \epsilon_{coup} \tag{72}$$

where ϵ_{coup} is a coupling tolerance. In practice, 2–3 sub-iterations typically suffice for the problems considered herein.

(iii) *Energy-based monitoring:* The total system energy can be monitored to detect coupling instabilities:

$$\mathcal{E}_{tot} = \int_{\Omega} \left[\psi(\boldsymbol{\epsilon}, s) + \frac{1}{2} \mathbb{s} p^2 \right] d\Omega \tag{73}$$

Non-physical energy growth indicates inadequate coupling resolution and triggers time step refinement.

For the numerical examples presented in Section 5, the combination of appropriately restricted time steps (satisfying Eq. (71)) and the ADR convergence criterion (Eq. (70) with $R_{tol} = 10^{-6}$) has proven sufficient to maintain coupling accuracy without requiring sub-iterations. The energy monitoring serves as a diagnostic tool to verify solution quality. In practice, with $R_{tol} = 10^{-6}$, the relative variation in total system energy between consecutive time steps remains below 0.1% during stable propagation phases.

5. Numerical examples

This section presents a comprehensive set of numerical examples designed to validate the proposed computational framework progressively, from individual model components to the fully coupled hydro-mechanical system. The performance of the developed approach is assessed through systematic comparisons against analytical solutions, established benchmark results, and available numerical and experimental data. Within the DH-PD framework, the horizon size is determined by prescribing a fixed number of neighboring particles; in all examples herein, unless otherwise stated, this number is set to 15. The examples are organized as follows: Section 5.1 first establishes the convergence properties and discretization independence of the variational damage formulation through notched square specimens under mode-I and mode-II loading; Section 5.2 then validates the poroelastic coupling through Terzaghi's one-dimensional consolidation benchmark; Section 5.3 verifies the fluid flow model via the five-spot well pattern problem; Section 5.4 demonstrates the fracture initiation and propagation capabilities using a pressure-driven notched specimen; and Section 5.5 showcases the framework's ability to capture complex hydraulic fracture interactions with pre-existing natural discontinuities. Through these analyses, the accuracy, robustness, and predictive capabilities of the methodology are demonstrated.

5.1. Convergence study: Notched square specimen under tension and shear test

As a first validation case, a square plate featuring a single horizontal edge notch is analyzed under quasi-static mode-I (tension) and mode-II (shear) loading, as depicted in Fig. 6. For the tensile scenario, a monotonically increasing vertical displacement is applied to the top edge at a loading rate of $\dot{u} = 1 \times 10^{-6}$ mm/s, while the bottom edge remains fully constrained. In the shear scenario, horizontal displacement is imposed on the upper boundary at a loading rate of $\dot{u} = 1 \times 10^{-5}$ mm/s to induce a predominantly mode-II fracture state (Fig. 6). The material parameters employed throughout are: Young's modulus $E = 210$ GPa, Poisson's ratio $\nu = 0.3$, critical energy release rate $G_c = 2700$ J/m^2, and length-scale parameter $\ell = 0.0075$ mm.

To systematically assess the influence of spatial discretization on the predicted fracture response, four levels of particle refinement are considered, with inter-particle spacings $\Delta x = \ell/3$, $\ell/4$, $\ell/5$, and $\ell/6$. The computed damage and phase-field contours for two representative resolutions ($\Delta x = \ell/4$ and $\ell/6$) under tensile loading are presented in Fig. 7. At each resolution, both the damage and phase-field contours consistently capture a horizontal crack that nucleates at the notch tip and extends toward the opposing boundary. Crucially, the width of the localized damage zone is governed by the regularization length ℓ rather than by the inter-particle distance, thereby confirming that the predicted fracture pattern is free from spurious discretization dependence. Upon refinement, the damage profiles converge to a stable and well-defined diffuse band.

The damage distributions obtained under shear loading at the same two resolutions are shown in Fig. 8. Under mode-II conditions, the fracture path deviates from the horizontal notch orientation and propagates along a curved trajectory toward the lower-right corner of the domain, consistent with well-established theoretical expectations for this benchmark configuration. The predicted crack path and the extent of the process zone remain in close agreement across all resolutions considered. Notably, the present variational damage formulation yields a markedly narrower localization band compared with the classical AT2 phase-field model at equivalent values of ℓ. This enhanced sharpness arises from the distinct scaling behavior: the damage bandwidth scales linearly with ℓ in the current approach, as opposed to the $\sqrt{\ell}$ scaling characteristic of the AT2 regularization (see Section 3 for a detailed discussion).

The mechanical response is further examined through force–displacement (F–u) curves. Fig. 9(a) compares these curves for all four discretization levels under tensile loading. Once sufficient spatial resolution is achieved, both the peak load and the subsequent post-peak softening branch become practically indistinguishable among successive refinements. Minor deviations are only discernible near the peak region for the coarsest spacing ($\Delta x = \ell/3$); for $\Delta x \leq \ell/4$, the curves effectively overlap, attesting to the favorable convergence properties of the method. The corresponding shear loading results are reported in Fig. 9(b). While slight variations are observed at the coarsest discretization, the global structural response rapidly stabilizes upon refinement, confirming that the mode-II predictions are equally insensitive to the choice of particle spacing.

Collectively, these tension and shear test results provide compelling numerical evidence that the proposed variational damage framework achieves discretization-independent fracture predictions and, concurrently, yields substantially sharper crack representations than the standard AT2 phase-field approach.

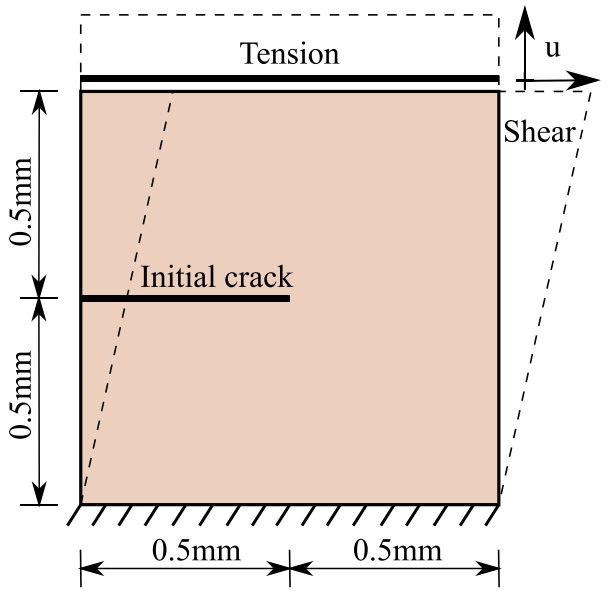

Fig. 6. Geometry and boundary conditions for the notched square.

Table 1
Material properties for the consolidation problem.

Parameters	Values	Parameters	Values
E (Pa)	1.0×10^{8}	ν	0
ℓ (m)	0.15	K_r, K_f (m^2)	1.0×10^{-12}
c_1	0.2	c_2	0.35
ρ_r, ρ_f (kg/m^3)	1.0×10^{3}	α_r, α_f	0.5
$\mathbb{s}_r$ (Pa^{-1})	1.65×10^{-10}	$\mathbb{s}_f$ (Pa^{-1})	1.65×10^{-11}
μ_r (Pa s)	1.0×10^{-3}	μ_f (Pa s)	1.0×10^{-3}

5.2. Terzaghi's consolidation benchmark

This example validates the fundamental poroelastic coupling mechanism within the proposed framework. Terzaghi's one-dimensional consolidation problem provides an ideal benchmark, as it involves the coupled interaction between pore pressure diffusion and solid skeleton deformation—the essential physics underlying any hydraulic fracturing model. Accurate reproduction of the analytical solution demonstrates that the nonlocal formulation correctly captures the bidirectional coupling between mechanical deformation and fluid flow.

The computational domain comprises a rectangular region with dimensions $L = 15$ m $\times$ $W = 1$ m, as depicted in Fig. 10. A uniform pressure of $P_0 = 10^4$ Pa is applied to the left boundary, whereas the right boundary remains fully constrained. For the hydraulic conditions, zero pressure (free drainage) is prescribed at the left edge, and impermeable (zero-flux) conditions are enforced along all remaining boundaries. The constitutive and transport parameters adopted for this analysis are summarized in Table 1.

The analytical solutions of this problem are available in the literature [58,59]:

$$p(x,t) = \frac{4\mathcal{V}P_0}{\pi}\sum_{i=0}^{N}\left\{\frac{1}{2i+1}\exp\left(-\left(\frac{(2i+1)\pi}{2L}\right)^2 Ct\right)\times\sin\left(\frac{(2i+1)\pi x}{2L}\right)\right\} \tag{74a}$$

$$u(x,t) = C_i\mathcal{V}P_0\left\{L-x-\frac{8L}{\pi^2}\sum_{i=0}^{N}\left\{\frac{1}{(2i+1)^2}\exp\left(-\left(\frac{(2i+1)\pi}{2L}\right)^2 Ct\right)\times\cos\left(\frac{(2i+1)\pi x}{2L}\right)\right\}\right\} + \mathcal{B}P_0(L-x) \tag{74b}$$

where the auxiliary coefficients are defined as $\mathcal{A} = 10^{-8}$ Pa, $\mathcal{B} = \mathcal{A}/(1+\mathcal{A}\alpha_f^2/\mathbb{s}_f)$, $\mathcal{V} = (\mathcal{A}-\mathcal{B})/(\mathcal{A}\alpha_f)$, $C = K_f/[(\mathcal{A}\alpha_f^2+\mathbb{s}_f)\mu_f]$, and $C_i = (\mathcal{A}-\mathcal{B})/\mathcal{V}$.

To validate the dual-horizon capability with spatially varying discretization, two spatial discretizations are considered: a uniform grid with particle spacing $\Delta x = 0.05$ m, and a graded particle distribution where the particle spacing varies from $\Delta x = 0.025$ m near the drainage boundary (where pressure gradients are steepest) to $\Delta x = 0.1$ m in the far field. Fig. 11 presents the computed pore pressure and displacement profiles along the specimen centerline at temporal instances $t = 15$, 30, 45, and 60 s. Excellent agreement

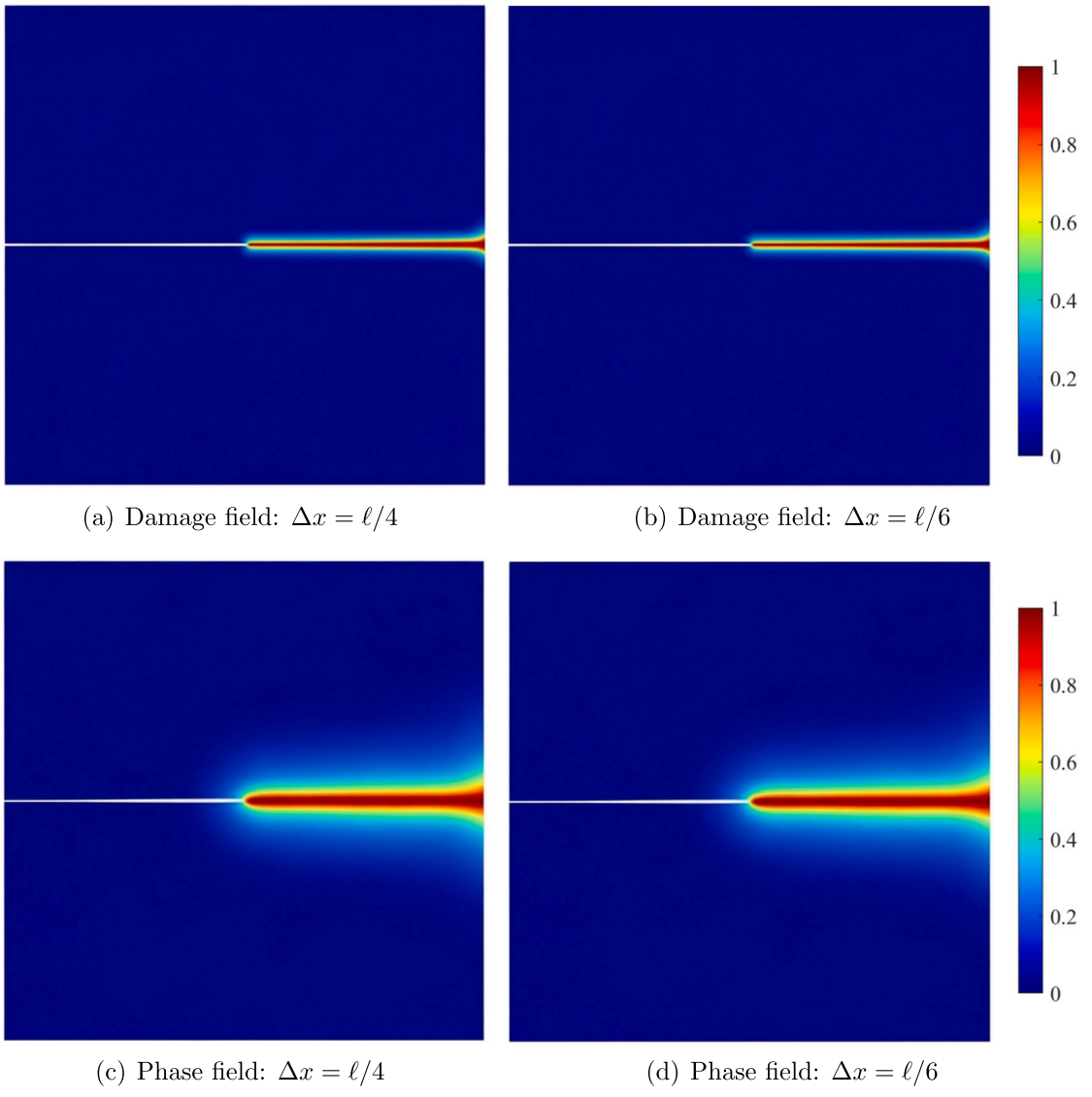

Fig. 7. Damage field and phase field for two discretization levels ($\Delta x = \ell/4$ and $\ell/6$) in the tension test.

is observed between the numerical results obtained from both discretizations and the corresponding analytical solutions, confirming that the proposed formulation accurately captures the poroelastic coupling behavior. In the graded discretization configuration, the dual-horizon formulation automatically handles the transition regions where neighboring particles possess different horizon sizes, without requiring any special treatment at the interface. This example substantiates the dual-horizon formulation's capacity to accommodate spatially varying discretization without compromising solution accuracy.

To assess discretization independence within the proposed framework, additional computations are conducted using particle spacings of $\Delta x = 0.01$ m, 0.025 m and 0.1 m. The comparative results illustrated in Fig. 12 demonstrate that varying spatial resolutions yield nearly identical solutions, all maintaining strong agreement with the analytical solutions. This convergence study confirms that the poroelastic coupling is robustly captured regardless of discretization refinement.

5.3. Five-spot well pattern simulation

This example validates the fluid flow component of the proposed formulation independently from fracture mechanics. The five-spot well pattern represents a classical petroleum engineering benchmark that tests the accuracy of pressure diffusion and fluid transport through porous media under steady-state conditions. Successful reproduction of the analytical pressure distribution confirms that the nonlocal gradient operators correctly model Darcy flow and that the source/sink treatment is properly implemented—essential prerequisites for accurate hydraulic fracturing simulations. The benchmark configuration, examined by

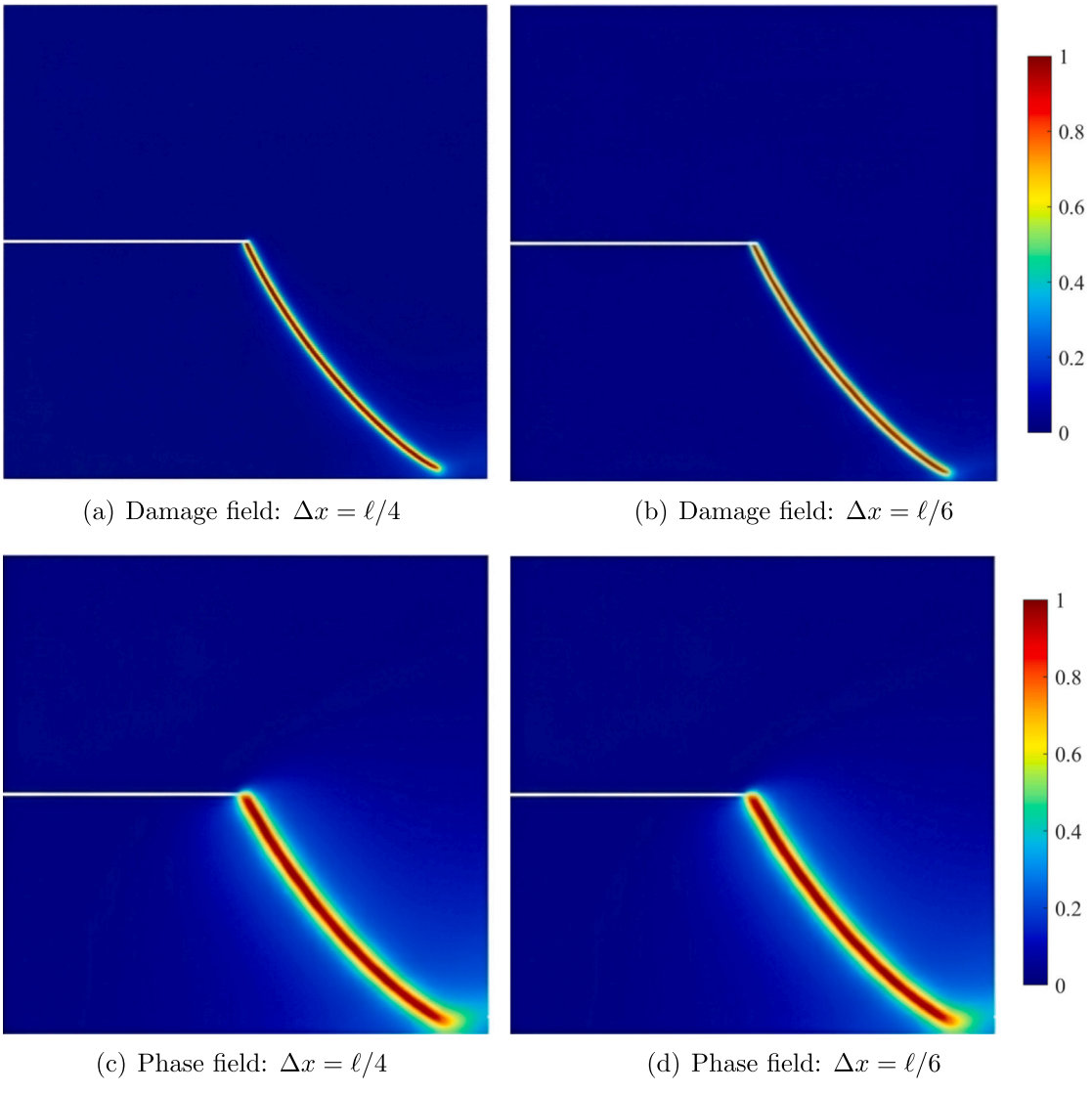

Fig. 8. Damage field and phase field for two discretization levels ($\Delta x = \ell/4$ and $\ell/6$) in the shear test.

Katiyar et al. [25], comprises four injection wells located at the vertices of a square domain with a single production well positioned at the center (Fig. 13(a)). The symmetric arrangement of injection and extraction rates ensures zero net flux across the domain boundaries. To reduce computational cost, the simulation is performed on the minimal repeating unit containing one injector-producer pair. No-flow and symmetry boundary conditions are imposed along the domain periphery, as illustrated in Fig. 13(b), with all external boundaries treated as impermeable.

Validation employs the steady-state analytical solution for pressure and flux induced by a point source of strength $\dot{Q}_n^i$ located at (x_i, y_i) within unit-thickness porous media [60]:

$$p_i(x,y) = -\frac{\dot{Q}_n^i \mu}{4\pi K} \ln\left[(x-x_i)^2 + (y-y_i)^2\right] + C_i \tag{75}$$

with integration constant C_i set to zero. Linear superposition yields the combined field from N point sources and sinks [60]:

$$p(x,y) = -\frac{\mu}{4\pi K} \sum_{i=1}^{N} \dot{Q}_n^i \ln\left[(x-x_i)^2 + (y-y_i)^2\right] \tag{76}$$

where N denotes the total number of source or sink points.

Exploiting central symmetry, the computational domain is reduced to a quarter section of dimensions $L \times L$. An injection well located at the origin $(0,0)$ maintains a constant pressure of 8 MPa, while a production well situated at (L,L) operates at -8 MPa.

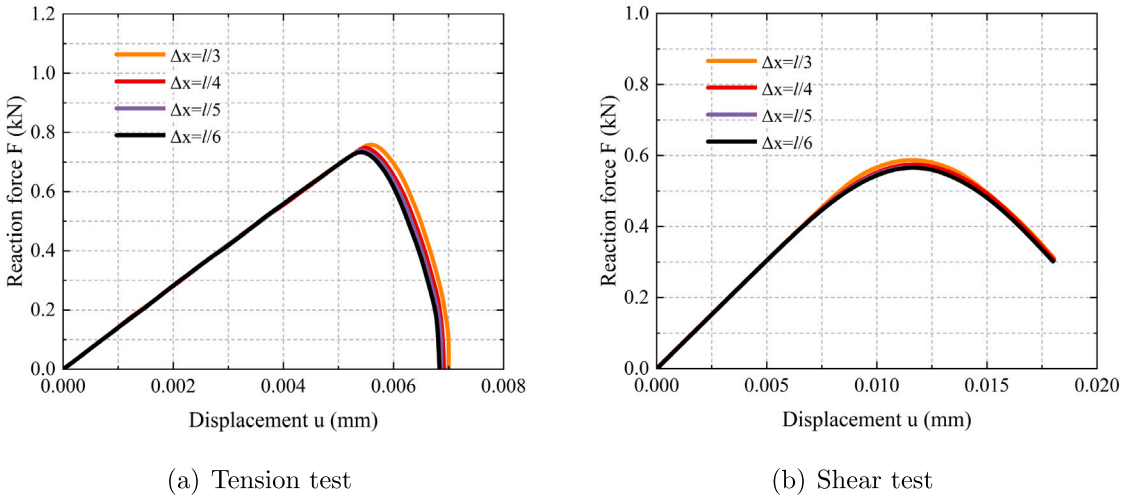

Fig. 9. Force–displacement curves for different discretization levels in the notched square tension and shear test.

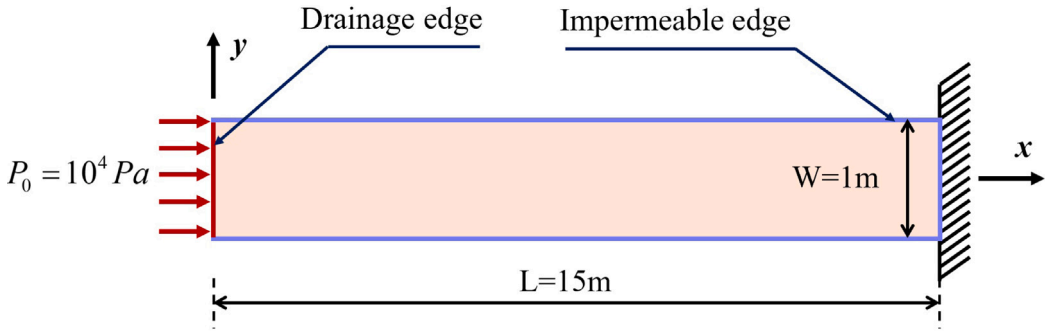

Fig. 10. Schematic representation of the consolidation problem.

Table 2
Material properties for the five-spot well pattern flow problem.

Parameters	Values	Parameters	Values
E (GPa)	10	ν	0.25
ℓ (m)	0.02	K_r, K_f (m^2)	1.0×10^{-13}
c_1	0.2	c_2	0.35
ρ_r, ρ_f (kg/m^3)	1.0×10^{3}	n_r	0.2
s_r (GPa^{-1})	1.0×10^{-11}	s_f (GPa^{-1})	0.47
μ_r (Pa s)	1.0×10^{-3}	μ_f (Pa s)	1.0×10^{-3}

Impermeable boundaries confine fluid flow exclusively to the porous formation between the source and sink. In this study, the square domain has a side length of $L = 1$ m and is discretized using a uniform grid with spacing $\Delta x = 0.005$ m. A total of 40,401 particles are initially distributed uniformly across the domain. The volumetric source term for each well is prescribed as $\dot{Q}_n^i = \pm 10^{-3}$ m^3/s. Following the approach in [25], the point source is regularized by distributing the volumetric source term $\dot{Q}_n^i$ over a characteristic smoothing length defined as

$$\lambda = 0.385\delta + 1.2925\Delta x \tag{77}$$

to mitigate numerical artifacts associated with pressure singularities at injection/production points. Within the support domain of radius λ, each neighboring material point receives a weighted source contribution given by

$$\mathscr{W} = \frac{\pi \dot{Q}_n}{\lambda^2(\pi^2 - 4)}\left[1 + \cos\left(\frac{\pi r}{\lambda}\right)\right] \tag{78}$$

where r denotes the distance from the point source to the neighboring point.

The complete set of simulation parameters is provided in Table 2.

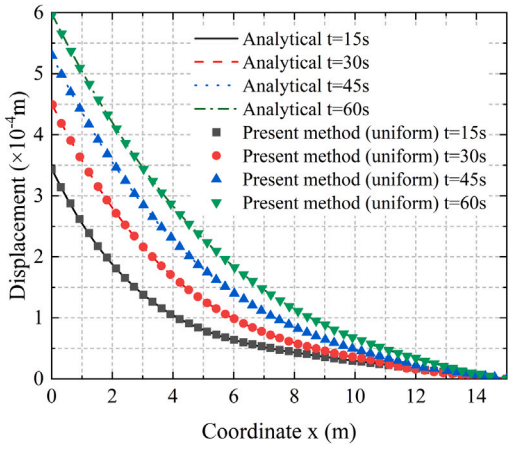

(a) Displacement field: uniform discretization

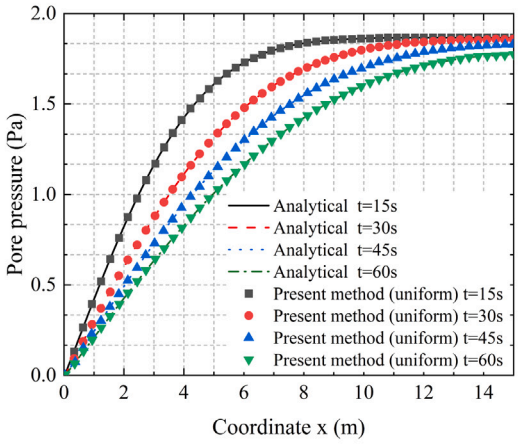

(b) Pore pressure field: uniform discretization

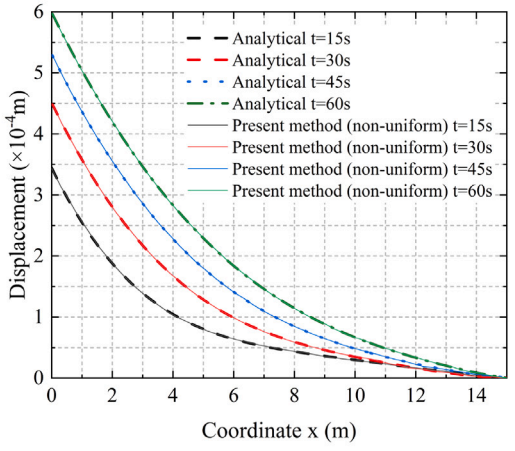

(c) Displacement field: non-uniform discretization

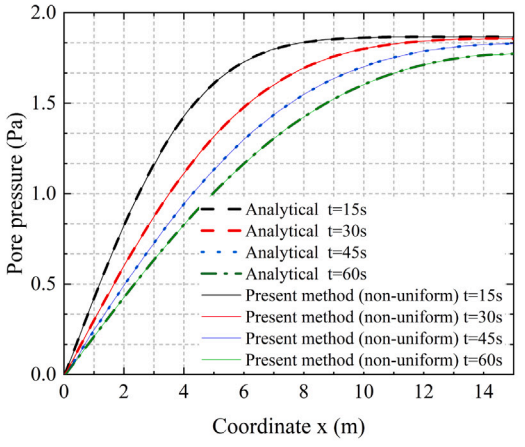

(d) Pore pressure field: non-uniform discretization

Fig. 11. Temporal evolution of displacement and pore pressure fields along the central axis: comparison between the analytical solution and the proposed method under different spatial discretizations.

Fig. 14(a)–(c) presents temporal snapshots of the pressure field contour evolution. Radial isobaric contours form around point sources, with elevated hydraulic gradients concentrated near well locations under high-pressure operation. The distribution progressively stabilizes over time. Comparison of the steady-state result against the previous numerical solution of [25] in Fig. 14(d) confirms good agreement. These results verify that the nonlocal fluid flow formulation accurately reproduces the expected pressure distribution in porous media.

Fig. 15 quantitatively compares diagonal pressure profiles connecting source and sink locations. Maximum and minimum extrema at well positions, together with interior pressure magnitudes, demonstrate excellent agreement with the classical analytical solutions, thereby validating the fluid transport modeling capability of the proposed framework.

5.4. Pressure-driven fracture initiation in a notched specimen

This example validates the fracture initiation and propagation capabilities of the proposed variational damage framework under hydraulic loading. Unlike the previous examples that tested poroelastic coupling and fluid flow separately, this benchmark examines the complete hydro-mechanical-damage coupling by simulating crack evolution from a pre-existing notch under progressively increasing fluid pressure. Comparison with the analytical crack-opening displacement solution and reference phase-field results demonstrates that the DH-PD formulation with variational damage correctly predicts both the onset and progression of hydraulic fractures.

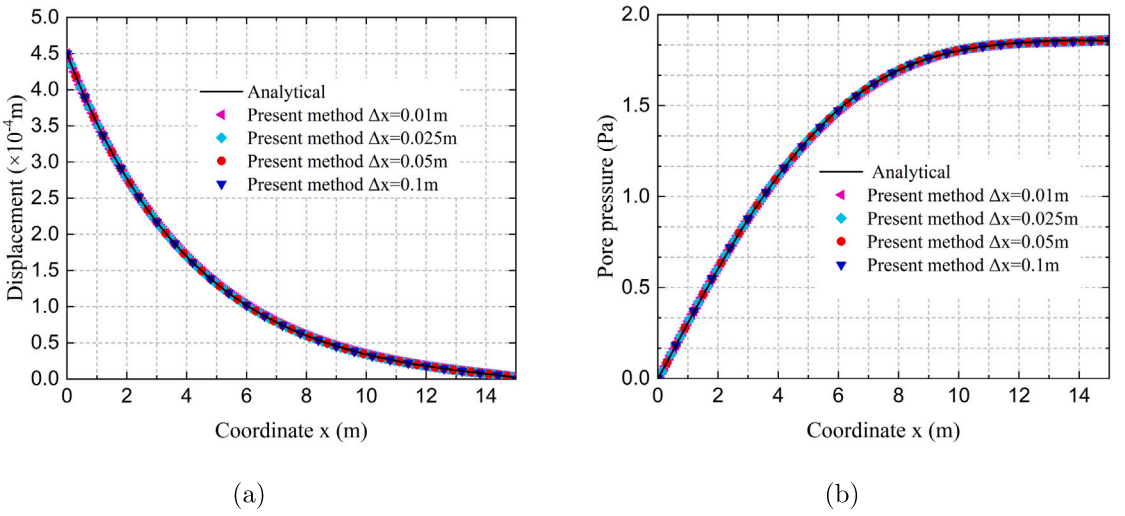

Fig. 12. Comparison between analytical and proposed model results at $t = 30$ s for various discretizations: (a) displacement and (b) pore pressure profiles along the central axis.

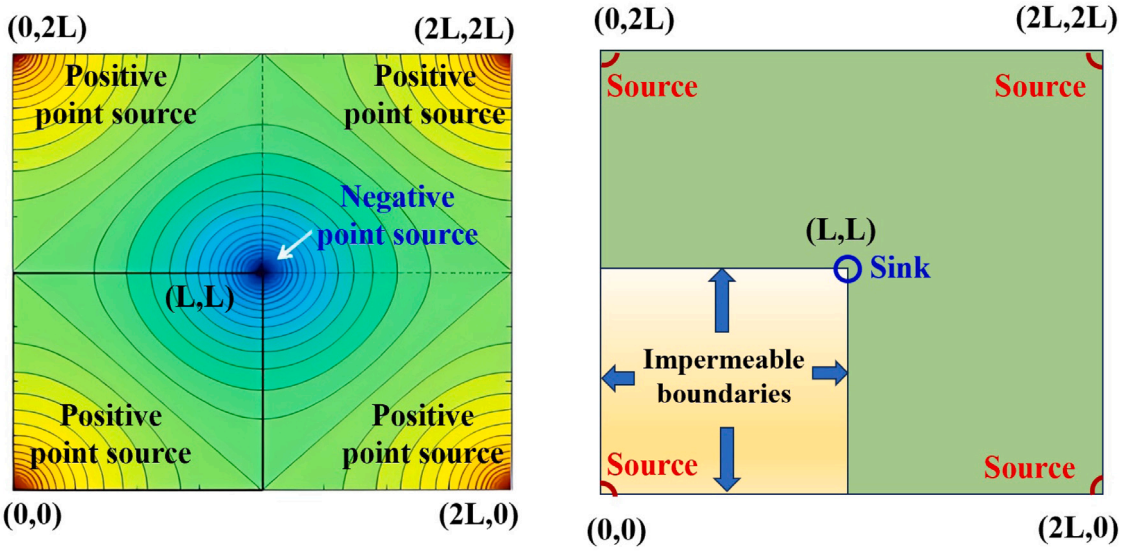

Fig. 13. Schematic of the confined five-spot well pattern [25], illustrating injection and production well positions within the computational domain.

Fig. 16(a) depicts the geometry and boundary prescriptions. A square specimen with dimensions $L \times L$ contains a horizontal pre-existing fracture of length $2l_c = 0.2$ m. Pressurized fluid $\bar{p}(t) = 5.5 \times 10^4 t$ (Pa) is introduced into the crack cavity while all external boundaries remain fully constrained with zero-pressure conditions imposed. Due to the inherent geometric symmetry, only half of the domain is discretized to enhance computational efficiency, as depicted in Fig. 16(b). Along the symmetry axis (left boundary), horizontal displacement constraints are enforced. Plane strain conditions are assumed throughout the analysis. Two distinct grid configurations are investigated for convergence assessment: the coarser discretization (Configuration 1) adopts a particle spacing of $\Delta x_1 = 5\times10^{-3}$ m, whereas the refined discretization (Configuration 2) employs $\Delta x_2 = 2.5\times10^{-3}$ m. Material constants and mechanical parameters adopted in this simulation are summarized in Table 3.

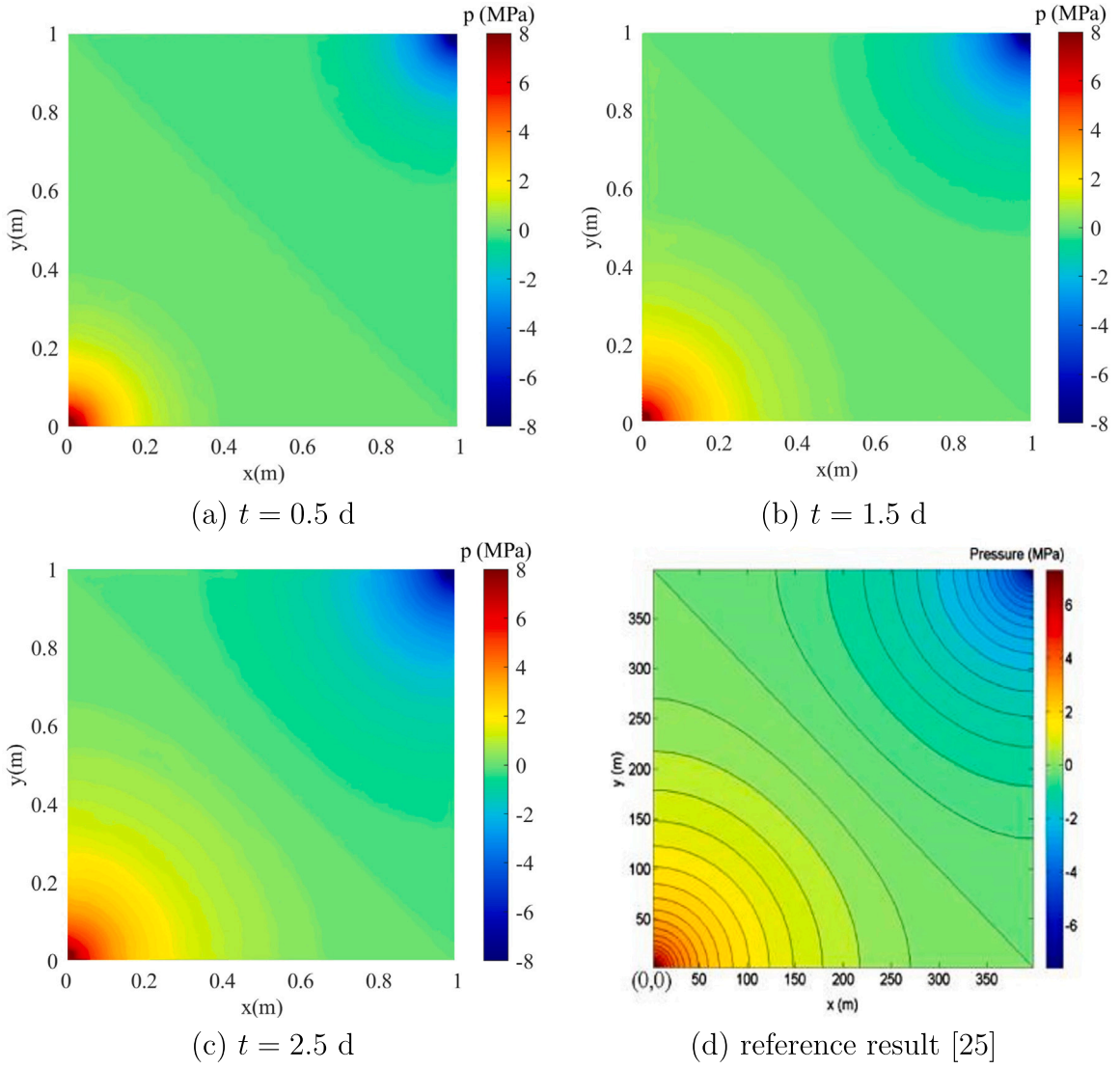

Fig. 14. Temporal evolution of the pressure contour from initial conditions to steady-state, with a comparison between the present steady-state result and the reference result of Katiyar et al. [25].

Table 3
Material and hydraulic parameters for the pressurized notched specimen.

Parameters	Values	Parameters	Values
E (GPa)	210	ν	0.25
G_c (J/m^2)	2700	k	1×10^{-9}
ℓ (m)	1.0×10^{-3}	c_1	0.5
c_2	1.0	$\mathfrak{m}_r$	2.0×10^{-3}
ρ_r, ρ_f (kg/m^3)	1.0×10^3	α	2.0×10^{-3}
Q_r (m^3/s)	0	Q_f (m^3/s)	0
K_r (m^2)	1×10^{-15}	K_f (m^2)	1.333×10^{-6}
$\mathfrak{s}_r$ (Pa^{-1})	1×10^{-8}	$\mathfrak{s}_f$ (Pa^{-1})	1×10^{-8}
μ_r (Pa s)	1×10^{-3}	μ_f (Pa s)	1×10^{-3}

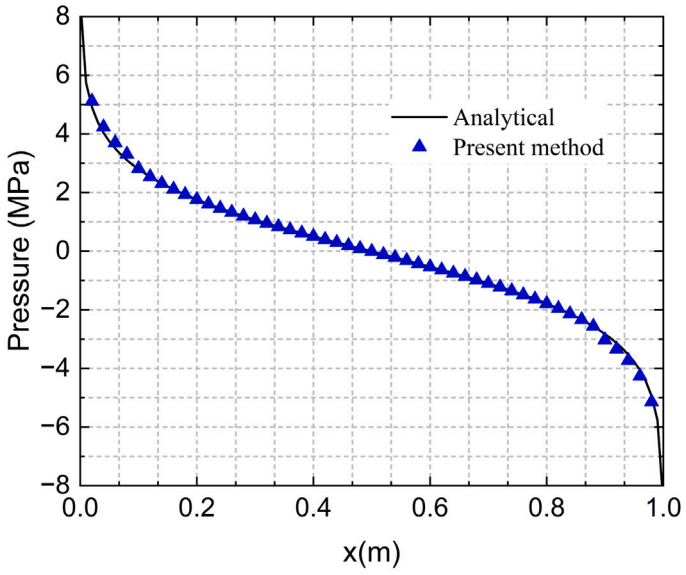

(a)

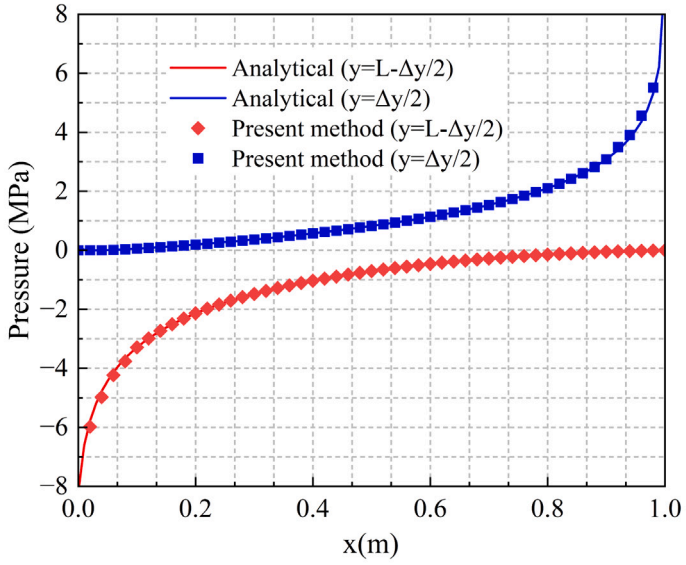

(b)

Fig. 15. Quantitative assessment of pressure distributions: (a) profile along the source–sink diagonal; (b) distributions along horizontal boundaries at $y = L - \Delta y/2$ and $y = \Delta y/2$.

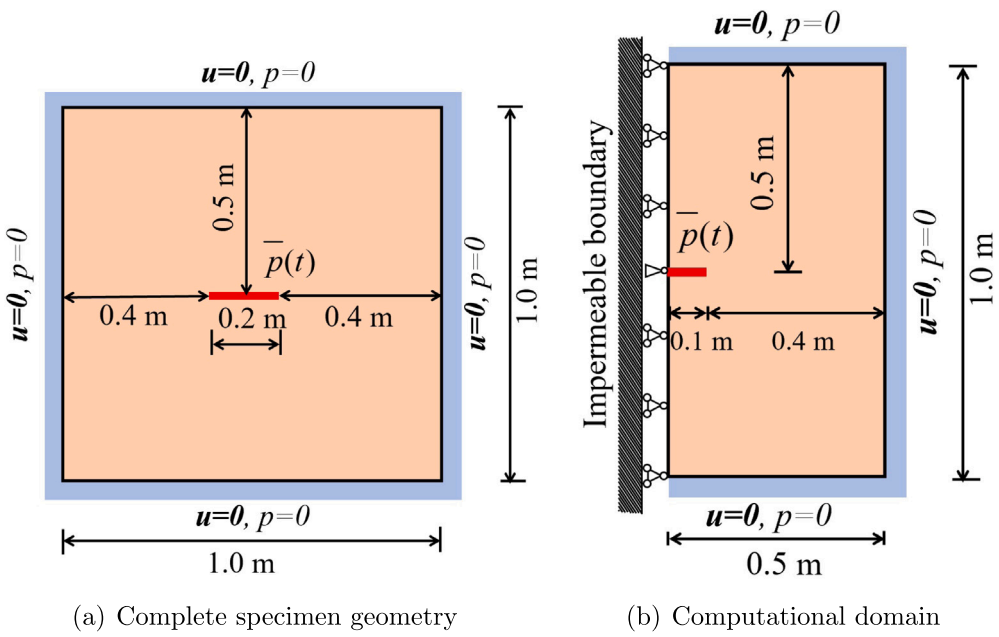

(a) Complete specimen geometry (b) Computational domain

Fig. 16. Problem configuration for the internally pressurized notched specimen.

For a fracture with half-length $l_c = 0.1$ m oriented along the $y = 0$ plane, the analytical solution for the vertical displacement field induced by a uniform internal pressure p is given by Sneddon and Lowengrub [61]:

$$u(x,p) = \frac{2pl_c}{E_p}\left(1 - \frac{x^2}{l_c^2}\right)^{1/2} \tag{79}$$

where $E_p = E/(1-\nu^2)$ denotes the plane-strain Young's modulus.

Fig. 17 compares the computed crack-opening profiles with analytical predictions for both discretizations. The finer discretization yields closer agreement with the theoretical solution, while both resolutions exhibit satisfactory correspondence. This agreement validates the accuracy of the proposed model in capturing the fundamental mechanics of pressure-driven fracture opening.

Progressive pressure elevation drives notch opening and horizontal crack extension. Figs. 18 and 19 show the damage field s and concurrent pressure distribution at different time instants. Crack aperture remains relatively constant throughout propagation. Peak pressure localizes within the fracture zone, with radial diffusion patterns evident. The substantially reduced pressure gradient parallel to the crack compared with the transverse direction ensures approximately uniform pressure distribution along the propagating fracture. The predicted crack trajectory and pressure distributions demonstrate good agreement with the phase-field simulation results reported in [53]. This validation confirms that the developed coupled framework is capable of accurately capturing the hydraulic fracturing mechanism, including both the initiation criterion and the subsequent propagation behavior.

5.5. Hydraulic fracture interaction with natural discontinuity networks

Having validated the individual components of poroelastic coupling, fluid flow, and fracture initiation/propagation in the preceding examples, this final set of simulations demonstrates the framework's capability to model complex, practically relevant hydraulic fracturing scenarios involving interactions with pre-existing natural discontinuities. These examples showcase the integrated performance of all coupled physics – fluid injection, pressure diffusion, mechanical deformation, damage evolution, and fracture-network interactions – representing the ultimate test of the proposed methodology for realistic subsurface applications. The configurations presented here are inspired by the analogous examples reported in Ni et al. [29], adapted to the present DH-PD framework with variational damage. Minor modifications to the domain dimensions have been introduced to ensure compatibility with the uniform particle spacing adopted in our discretization, as detailed below.

The complete specimen geometry, computational domain configurations, and associated boundary prescriptions for two representative scenarios are illustrated in Fig. 20. In the first scenario, a horizontal pre-existing crack with an initial length of $l = 0.3$ m is positioned at the geometric center of the specimen. The second scenario incorporates two additional vertical natural fractures extending 1 m in length, enabling a systematic investigation of the interaction mechanisms between propagating hydraulic fractures and pre-existing discontinuities. Fracturing fluid enters the system through the midpoint of the horizontal discontinuity at a prescribed volumetric flux of $Q = 1 \times 10^{-3}$ m^3/s. The computational domain is discretized using a uniform grid with spacing $\Delta x = 0.01$ m. The material constants and fluid properties employed throughout these analyses are summarized in Table 4.

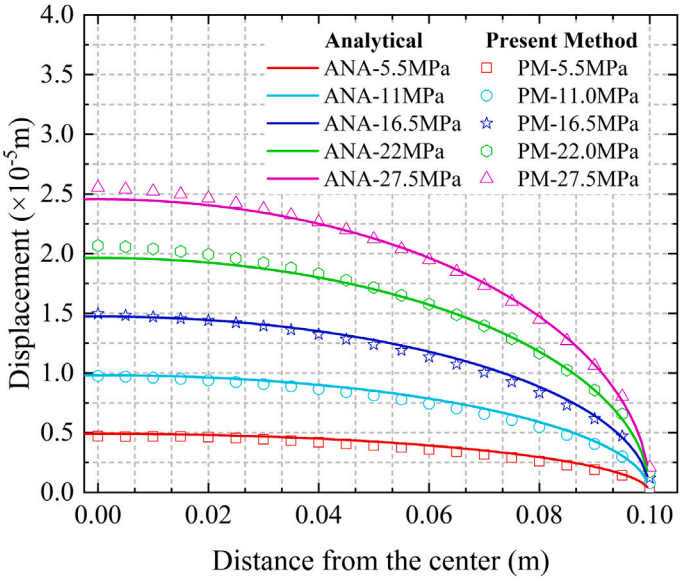

(a) Configuration 1

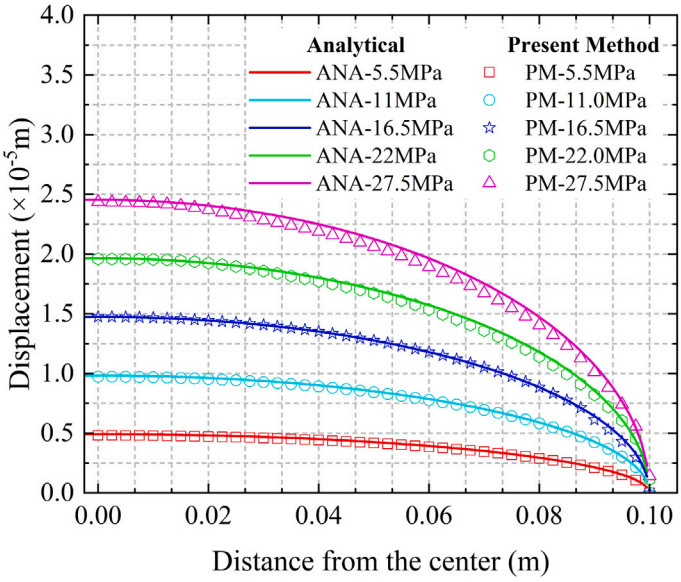

(b) Configuration 2

Fig. 17. Crack-opening displacement profiles: comparison of numerical results (symbols) against the analytical solution (curves) for two discretization levels.

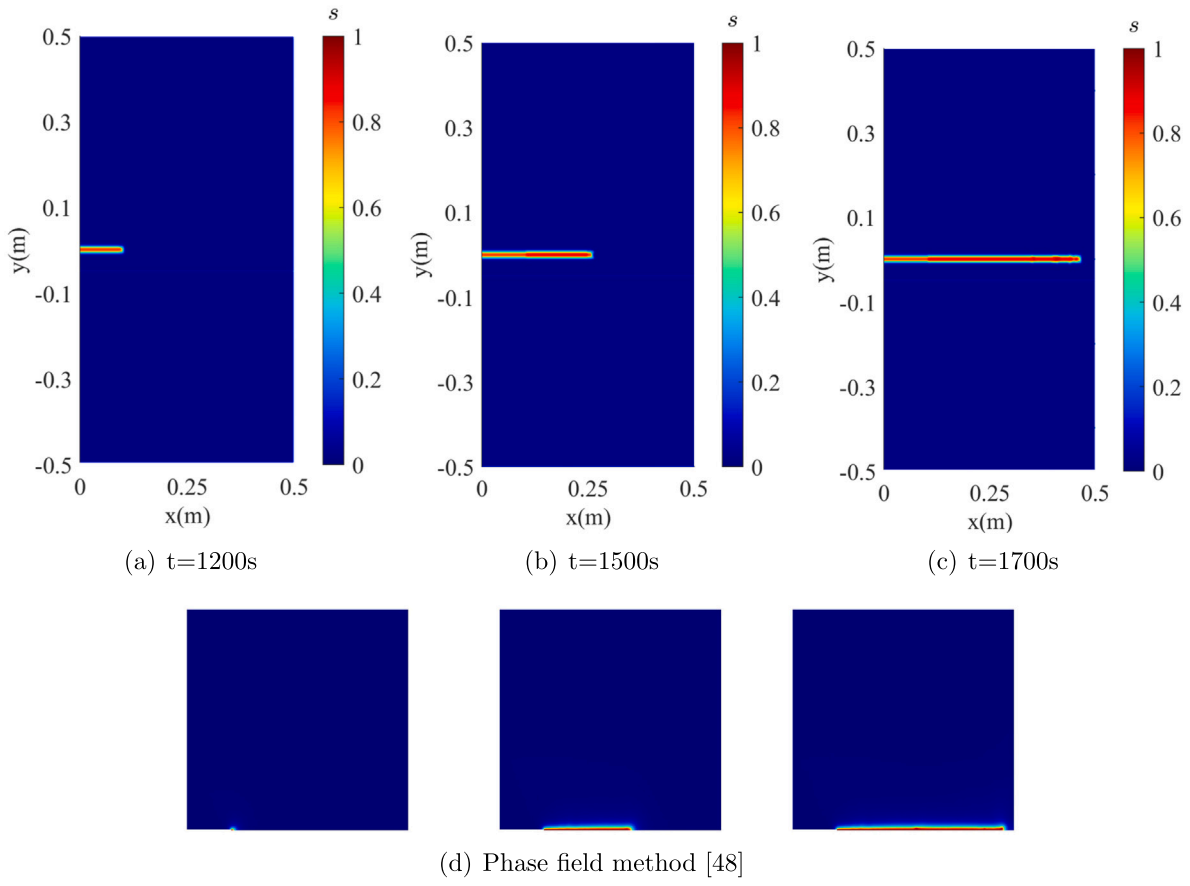

Fig. 18. Comparison of crack propagation paths between the present method (a)–(c) and the phase-field method (d) [53].

Table 4
Material and hydraulic properties for natural fracture interaction simulations.

Parameters	Values	Parameters	Values
E (GPa)	0.1	ν	0.25
G_c (J/m^2)	100	k	1×10^{-9}
ℓ (m)	3×10^{-2}	c_1	0.5
c_2	1.0	$\mathfrak{n}_r$	0.4
ρ_r, ρ_f (kg/m^3)	1×10^{3}	α	1.0
K_r (m^2)	1×10^{-12}	K_f (m^2)	1×10^{-12}
$\mathbb{s}_r$ (Pa^{-1})	1×10^{-10}	$\mathbb{s}_f$ (Pa^{-1})	1×10^{-10}
μ_r (Pa s)	1×10^{-3}	μ_f (Pa s)	1×10^{-3}

Figs. 21–22 illustrate the crack propagation and pressure field evolution for scenarios 1 and 2 throughout the hydraulic stimulation process. As the fracturing fluid is continuously injected into the system, it migrates along established flow pathways within the discontinuities, progressively elevating the pore pressure in adjacent regions. This pressure redistribution simultaneously induces solid skeleton deformation and promotes further crack advancement. The proposed computational framework effectively captures the coupled fracture propagation phenomena and characterizes fluid migration behavior within fractured saturated porous media through a physically consistent and mathematically rigorous approach.

The temporal evolution of fluid pressure at the injection point is illustrated in Fig. 23. The injection-point pressure histories are compared with the corresponding results reported in Ni et al. [29], demonstrating good qualitative and quantitative agreement in terms of the characteristic pressure responses, including the initial pressure buildup, the peak pressure at fracture initiation, and the subsequent pressure decline during crack propagation. Upon fluid injection, an abrupt pressure surge occurs, which progressively opens the pre-existing horizontal discontinuity and enhances local permeability, subsequently inducing rapid pressure dissipation. Initially, fluid migration exhibits isotropic behavior when the fracture aperture remains minimal (time instant A). As the discontinuity opens further, preferential flow along the fracture orientation becomes dominant (time instant B), eventually reaching approximate pressure equilibrium between the fracture tips and injection point (time instant C). Beyond instant C, hydraulic

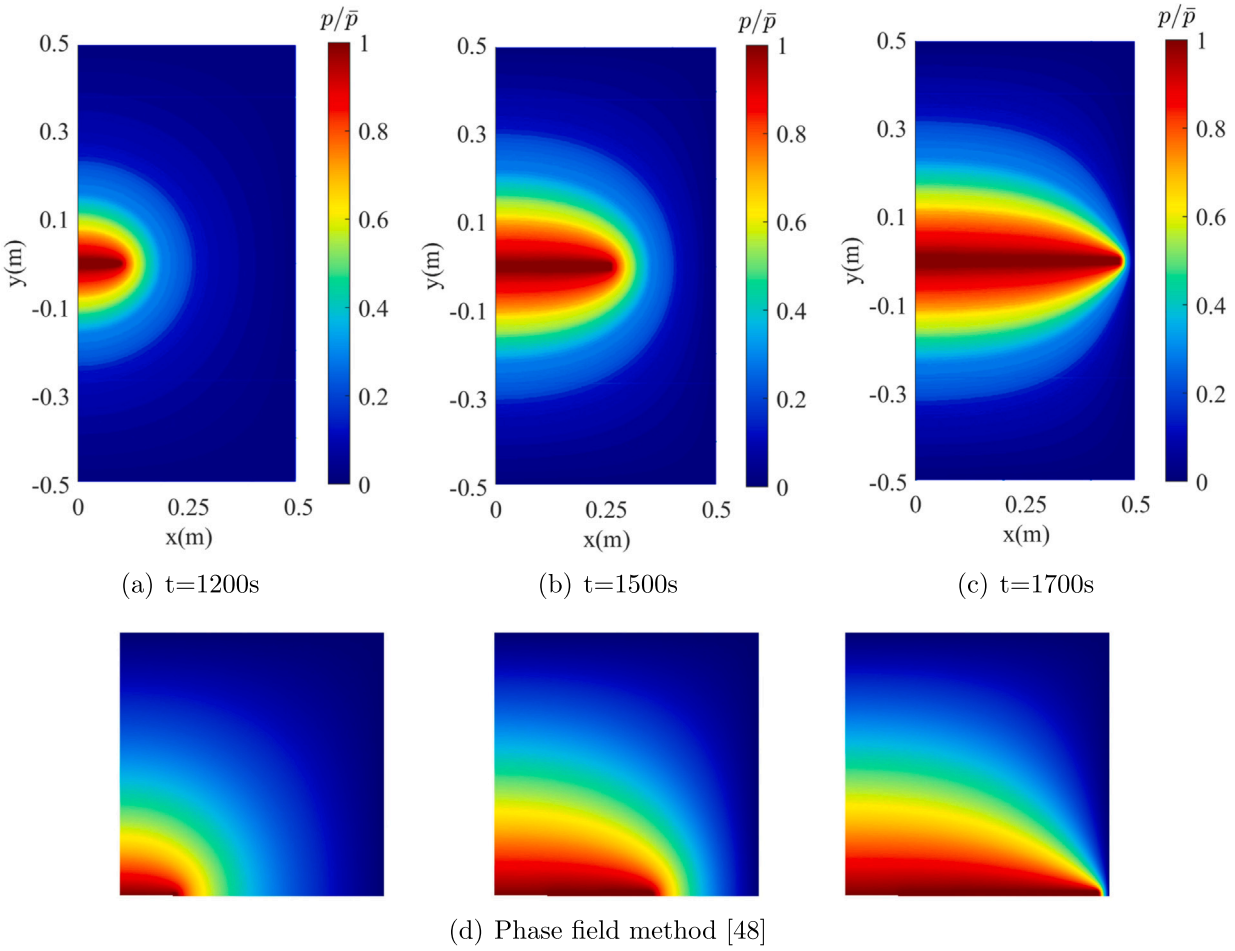

Fig. 19. Comparison of pressure field distributions obtained from the present approach (a)–(c) and the phase-field model (d) [53].

fracturing initiates across all scenarios, accompanied by modest pressure elevation during initial propagation followed by progressive reduction as fracture extension accelerates. In scenario 2, the intersection and activation of vertically oriented pre-existing discontinuities trigger an extremely rapid pressure decline (interval D–E). Subsequently, pressure within the vertical discontinuities gradually recovers until secondary cracks nucleate from their extremities and propagate toward the domain boundaries. Upon fracture breakthrough to the zero-pressure boundaries, another precipitous pressure reduction occurs (beyond instant F).

To investigate the influence of injection rate on fracture morphology, additional simulations are conducted using the Scenario 1 geometry with progressively increased rates: Scenario 1-1 ($Q = 2 \times 10^{-3}$ m^3/s), Scenario 1-2 ($Q = 4 \times 10^{-3}$ m^3/s), and Scenario 1-3 ($Q = 6 \times 10^{-3}$ m^3/s). Fig. 24(a)–(c) present the resulting crack patterns at the final stage, with corresponding pressure distributions shown in panels (d)–(f). Higher injection rates promote crack bifurcation, a phenomenon characteristic of dynamic hydraulic fracturing. This capability to capture injection-rate-dependent fracture branching demonstrates the framework's utility for optimizing stimulation treatments. Fig. 25 illustrates the pressure evolution histories for all injection rates considered. As highlighted in the magnified regions of Fig. 25, pronounced pressure oscillations are observed during fracturing events. This behavior is consistent with experimental observations reported by Lhomme et al. [62] and numerical findings of Cao et al. [63], further validating the physical fidelity of the proposed approach.

All simulations are performed on a workstation equipped with an Intel Xeon processor. For the Terzaghi consolidation problem, the computation requires approximately 15 min with $\Delta x = 0.05$ m. The five-spot well pattern simulation takes approximately 45 min to reach steady state. For the pressure-driven fracture problem, the computational times are approximately 2.5 h (Configuration 1) and 8 h (Configuration 2). The complex fracture interaction examples require approximately 6–12 h depending on the scenario and injection rate. These timings reflect the explicit time integration scheme adopted in this work, and significant speedup could be achieved through parallelization, which is planned as future work.

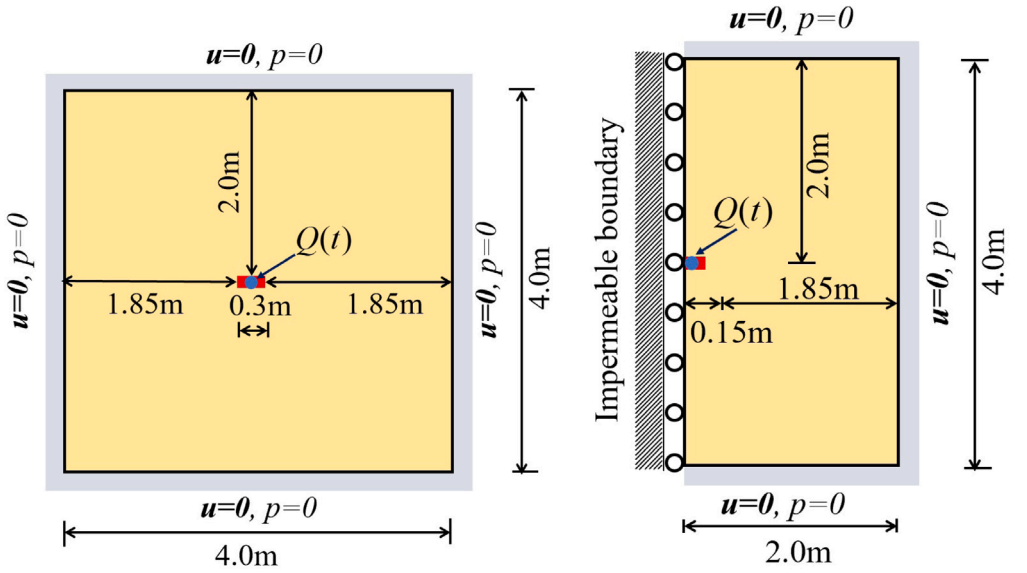

(a) Scenario 1: Complete specimen geometry (b) Scenario 1: Computational domain

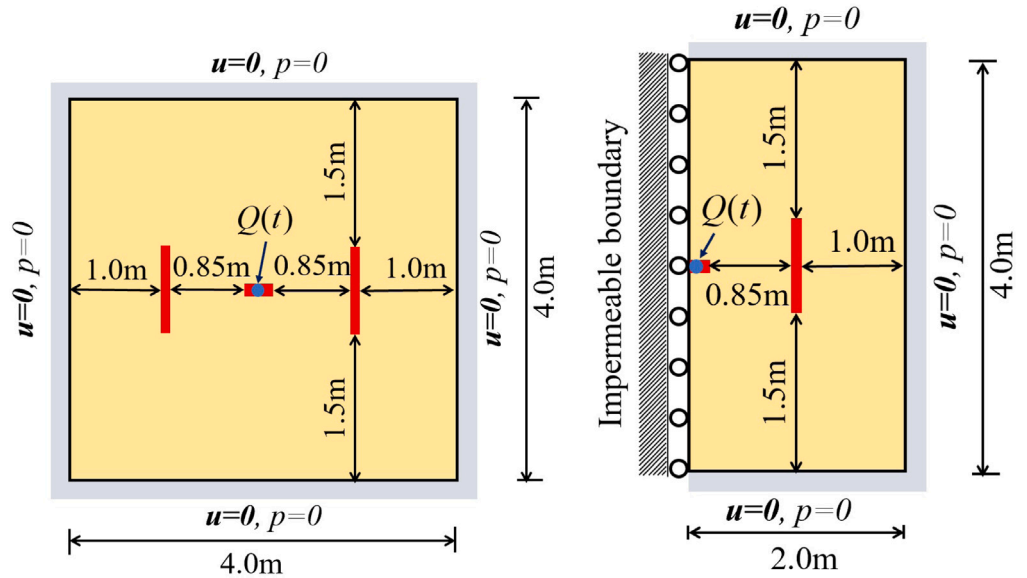

(c) Scenario 2: Complete specimen geometry (d) Scenario 2: Computational domain

Fig. 20. Geometric configurations and boundary conditions for two hydraulic fracturing scenarios with natural discontinuities.

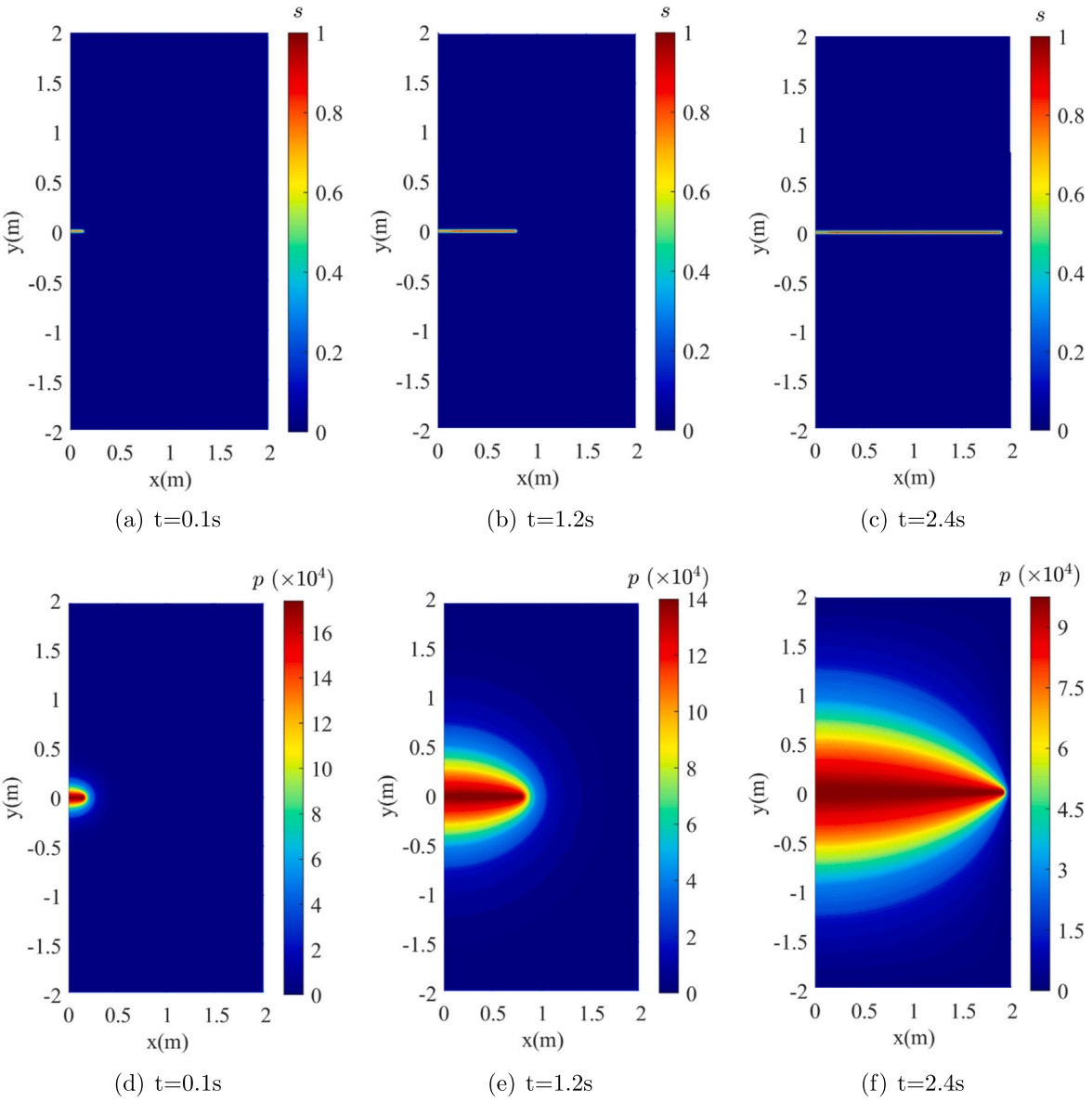

Fig. 21. Scenario 1: Crack propagation and pressure field evolution during unimpeded horizontal fracture propagation.

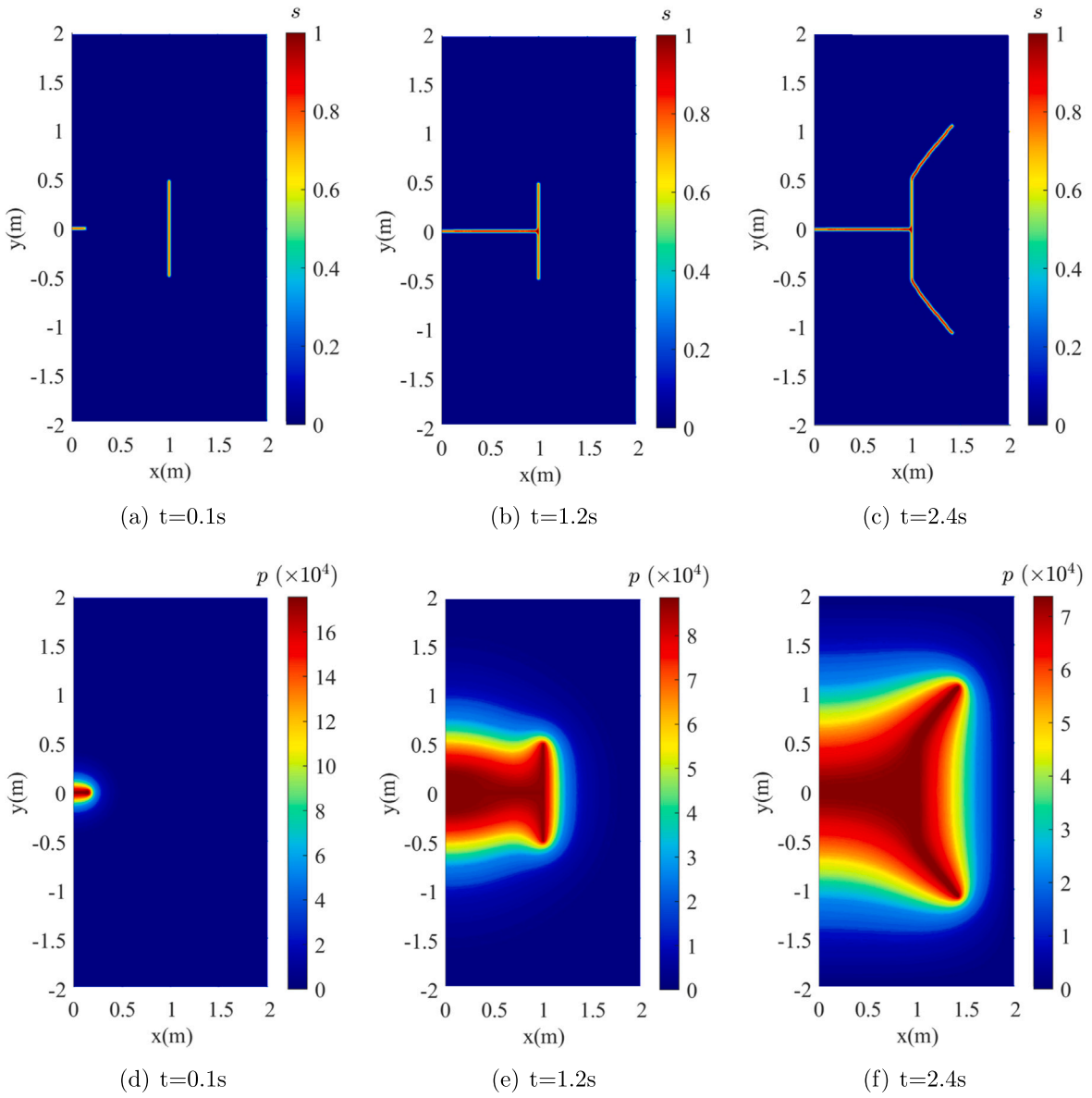

Fig. 22. Scenario 2: Crack propagation and pressure field evolution in the presence of multiple vertical natural discontinuities.

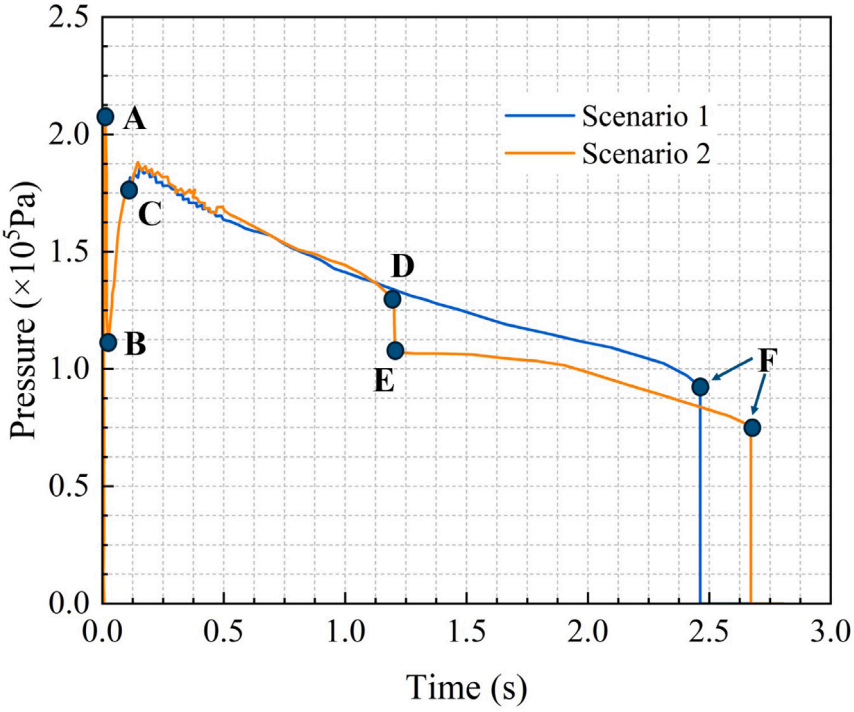

Fig. 23. Temporal evolution of injection-point pressure for both scenarios, with magnified insets highlighting characteristic pressure events.

6. Conclusions

A comprehensive computational methodology for hydraulic fracture simulation in brittle saturated porous media has been developed by integrating DH-NOSBPD with variational damage theory. The main contributions and outcomes of this investigation are recapitulated below:

1. A DH-PD formulation for hydro-mechanically coupled problems has been rigorously developed, wherein both mechanical equilibrium and pore pressure diffusion equations are derived using consistent nonlocal gradient operators. This formulation inherently accommodates non-uniform spatial discretization and adaptive refinement while ensuring strict conservation of momentum and energy.
2. The integration of variational damage theory within the dual-horizon framework eliminates the need for phenomenological bond-breaking criteria. Damage evolution emerges naturally from energy minimization principles, thereby providing a physically consistent mechanism for fracture nucleation and propagation under combined mechanical and hydraulic loading conditions.
3. A unified treatment of pore fluid transport through intact porous media and evolving fracture networks has been achieved by formulating the pressure diffusion equation with nonlocal operators consistent with the mechanical formulation. The damage-dependent permeability model enables smooth transitions between matrix and fracture flow regimes without explicit crack aperture tracking.
4. An efficient staggered solution algorithm has been developed that combines adaptive dynamic relaxation for attaining quasi-static mechanical equilibrium with explicit time integration for fluid pressure evolution. This approach effectively addresses the disparate time scales inherent in hydro-mechanical coupling while maintaining numerical stability.
5. The predictive capabilities of the proposed framework have been demonstrated through comprehensive numerical examples, including pressure-driven fracture initiation, fluid-induced crack propagation, fracture branching and coalescence, and hydraulic fracture interaction with pre-existing natural discontinuities. Systematic convergence studies and comparisons with analytical solutions confirm the accuracy and predictive capability of the methodology.

The developed framework offers a robust and versatile computational tool for investigating hydraulic fracturing phenomena. The elimination of explicit crack tracking, combined with physically grounded damage evolution, provides distinct advantages over conventional approaches, particularly for problems involving complex fracture patterns, adaptive discretization, and strong hydro-mechanical coupling, where phenomenological criteria may introduce spurious artifacts. Future research directions include extension to three-dimensional configurations with efficient parallel implementations, incorporation of additional physical mechanisms such as thermal effects and multiphase flow [64–66], and development of adaptive refinement strategies specifically tailored to coupled hydro-mechanical-damage systems.

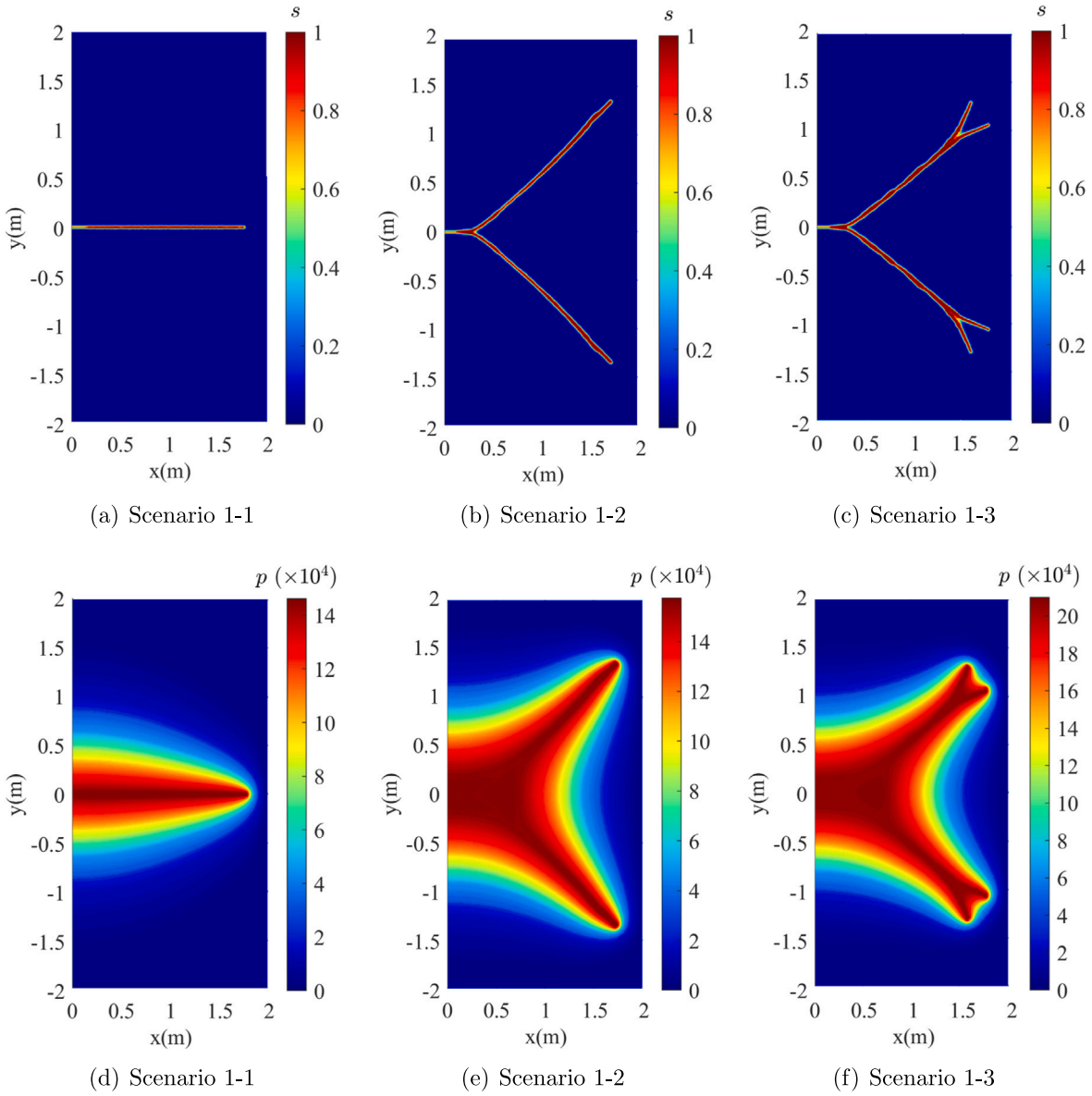

(a) Scenario 1-1 (b) Scenario 1-2 (c) Scenario 1-3

(d) Scenario 1-1 (e) Scenario 1-2 (f) Scenario 1-3

Fig. 24. Crack patterns (a)–(c) and corresponding pressure distributions (d)–(f) at the final stage for scenario 1 under various injection rates.

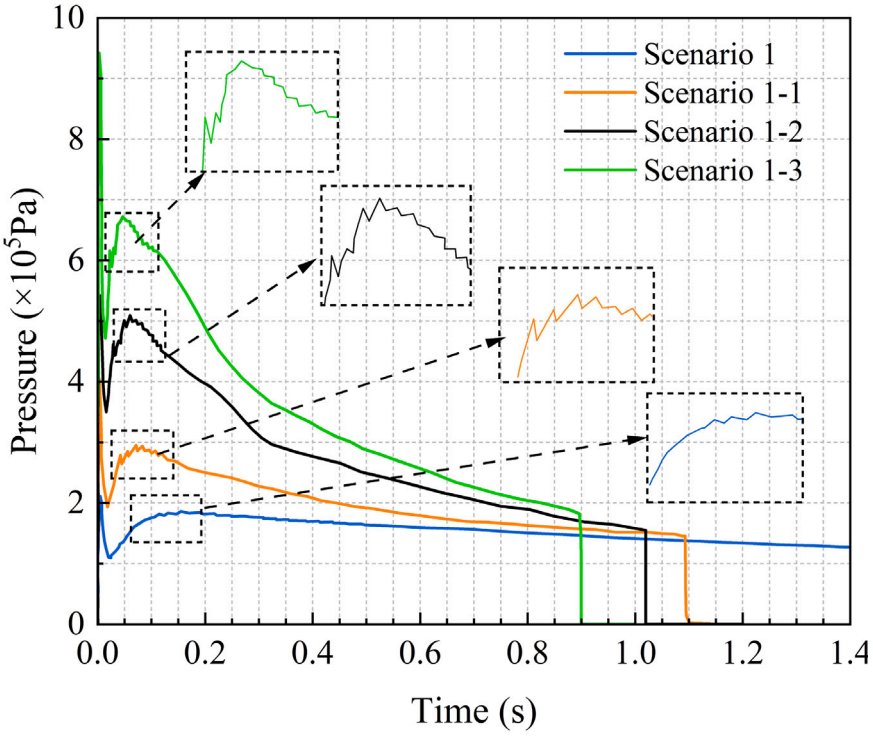

Fig. 25. Injection-point pressure histories for Scenarios 1, 1-1, 1-2, and 1-3 with magnified insets illustrating oscillatory responses during crack propagation.

CRediT authorship contribution statement

Yongzheng Zhang: Writing – original draft, Software, Methodology, Investigation, Data curation, Conceptualization. **Jidong Zhao:** Writing – review & editing, Supervision, Resources, Project administration. **Gang Wang:** Supervision, Resources, Funding acquisition. **Xuxu Yang:** Visualization, Validation, Investigation. **Timon Rabczuk:** Writing – review & editing, Supervision, Methodology, Investigation.

Declaration of competing interest

The authors declare that they have no known competing financial interests or personal relationships that could have appeared to influence the work reported in this paper.

Acknowledgments

The authors gratefully acknowledge financial support from the Postdoctoral Innovative Talents Support Program (GZC20240950), the National Natural Science Foundation of China (52478390 and 52439001), the China Postdoctoral Science Foundation (2023M7 42145), the Shandong Province Postdoctoral International Exchange Program (202401026), the Qingdao Postdoctoral Science Foundation (QDBSH20230202119), the Research Grants Council of Hong Kong (16212724), the State Key Laboratory of Climate Resilience for Coastal Cities (Project ITC-SKLCRCC26EG01), and the Shandong Youth Innovation Technology Support Program (2023KJ092).

Data availability

Data will be made available on request.

References

[1] Emmanuel Detournay, Mechanics of hydraulic fractures, Annu. Rev. Fluid Mech. 48 (2016) 311–339.
[2] Pierre M. Adler, Jean-François Thovert, Valeri V. Mourzenko, Fractured Porous Media, Oxford University Press, 2013.
[3] Maurice A. Biot, General theory of three-dimensional consolidation, J. Appl. Phys. 12 (2) (1941) 155–164.
[4] Olivier Coussy, Poromechanics, John Wiley & Sons, 2004.
[5] Paul A. Witherspoon, Joseph S.Y. Wang, Kazuhiko Iwai, John E. Gale, Validity of cubic law for fluid flow in a deformable rock fracture, Water Resour. Res. 16 (6) (1980) 1016–1024.
[6] Robert W. Zimmerman, Gudmundur S. Bodvarsson, Hydraulic conductivity of rock fractures, Transp. Porous Media 23 (1) (1996) 1–30.
[7] Nicolas Moës, John Dolbow, Ted Belytschko, A finite element method for crack growth without remeshing, Internat. J. Numer. Methods Engrg. 46 (1) (1999) 131–150.
[8] Ted Belytschko, Robert Gracie, Giulio Ventura, A review of extended/generalized finite element methods for material modeling, Modelling Simul. Mater. Sci. Eng. 17 (4) (2009) 043001.
[9] Christian Miehe, Martina Hofacker, Fabian Welschinger, A phase field model for rate-independent crack propagation: Robust algorithmic implementation based on operator splits, Comput. Methods Appl. Mech. Engrg. 199 (45–48) (2010) 2765–2778.
[10] Christian Miehe, Martina Hofacker, Fabian Welschinger, Thermodynamically consistent phase-field models of fracture: Variational principles and multi-field FE implementations, Internat. J. Numer. Methods Engrg. 83 (10) (2010) 1273–1311.
[11] Michael J. Borden, Clemens V. Verhoosel, Michael A. Scott, Thomas J.R. Hughes, Chad M. Landis, A phase-field description of dynamic brittle fracture, Comput. Methods Appl. Mech. Engrg. 217–220 (2012) 77–95.
[12] Grigory I. Barenblatt, The mathematical theory of equilibrium cracks in brittle fracture, Adv. Appl. Mech. 7 (1962) 55–129.
[13] Donald S. Dugdale, Yielding of steel sheets containing slits, J. Mech. Phys. Solids 8 (2) (1960) 100–104.
[14] Peter A. Cundall, Otto D.L. Strack, A discrete numerical model for granular assemblies, Géotechnique 29 (1) (1979) 47–65.
[15] Andrea Lisjak, Giovanni Grasselli, A review of discrete modeling techniques for fracturing processes in discontinuous rock masses, J. Rock Mech. Geotech. Eng. 6 (4) (2014) 301–314.
[16] Timon Rabczuk, Ted Belytschko, Cracking particles: A simplified meshfree method for arbitrary evolving cracks, Internat. J. Numer. Methods Engrg. 61 (13) (2004) 2316–2343.
[17] Stewart A. Silling, Reformulation of elasticity theory for discontinuities and long-range forces, J. Mech. Phys. Solids 48 (1) (2000) 175–209.
[18] Stewart A. Silling, Richard B. Lehoucq, Peridynamic theory of solid mechanics, Adv. Appl. Mech. 44 (2010) 73–168.
[19] Youn Doh Ha, Florin Bobaru, Studies of dynamic crack propagation and crack branching with peridynamics, Int. J. Fract. 162 (1–2) (2010) 229–244.
[20] Stewart A. Silling, Michael Epton, Olaf Weckner, Jifeng Xu, Ebrahim Askari, Peridynamic states and constitutive modeling, J. Elasticity 88 (2) (2007) 151–184.
[21] Florin Bobaru, Mijia Yang, Leonardo Frota Alves, Stewart A. Silling, Ebrahim Askari, Jifeng Xu, Convergence, adaptive refinement, and scaling in 1D peridynamics, Internat. J. Numer. Methods Engrg. 77 (6) (2009) 852–877.
[22] Greta Ongaro, Arman Shojaei, Farshid Mossaiby, Alexander Hermann, Christian J. Cyron, Patrizia Trovalusci, Multi-adaptive spatial discretization of bond-based peridynamics, Int. J. Fract. 244 (1) (2023) 1–24.
[23] Huilong Ren, Xiaoying Zhuang, Yongchang Cai, Timon Rabczuk, Dual-horizon peridynamics, Internat. J. Numer. Methods Engrg. 108 (12) (2016) 1451–1476.
[24] Selda Oterkus, Erdogan Madenci, Erkan Oterkus, Fully coupled poroelastic peridynamic formulation for fluid-filled fractures, Eng. Geol. 225 (2017) 19–28.
[25] Amit Katiyar, John T. Foster, Hisanao Ouchi, Mukul M. Sharma, A peridynamic formulation of pressure driven convective fluid transport in porous media, J. Comput. Phys. 261 (2014) 209–229.
[26] Hisanao Ouchi, Amit Katiyar, Jason York, John T. Foster, Mukul M. Sharma, A fully coupled porous flow and geomechanics model for fluid driven cracks: A peridynamics approach, Comput. Mech. 55 (3) (2015) 561–576.
[27] Daniel Z. Turner, A non-local model for fluid-structure interaction with applications in hydraulic fracturing, Int. J. Comput. Methods Eng. Sci. Mech. 14 (5) (2013) 391–400.
[28] Yanan Sun, Bin Chen, Michael G. Edwards, Investigation of hydraulic fracture branching in porous media with a hybrid finite element and peridynamic approach, Theor. Appl. Fract. Mech. 116 (2021) 103133.
[29] Tao Ni, Francesco Pesavento, Mirco Zaccariotto, Ugo Galvanetto, Qi-Zhi Zhu, Bernhard A. Schrefler, Hybrid FEM and peridynamic simulation of hydraulic fracture propagation in saturated porous media, Comput. Methods Appl. Mech. Engrg. 366 (2020) 113101.
[30] Shahla Nadimi, Ilija Miscovic, John McLennan, A 3D peridynamic simulation of hydraulic fracture process in a heterogeneous medium, J. Pet. Sci. Eng. 145 (2016) 444–452.
[31] Hisanao Ouchi, Development of Peridynamics-Based Hydraulic Fracturing Model for Fracture Growth in Heterogeneous Reservoirs (Ph.D. thesis), The University of Texas at Austin, 2016.
[32] Gilles A. Francfort, Jean-Jacques Marigo, Revisiting brittle fracture as an energy minimization problem, J. Mech. Phys. Solids 46 (8) (1998) 1319–1342.
[33] Blaise Bourdin, Gilles A. Francfort, Jean-Jacques Marigo, Numerical experiments in revisited brittle fracture, J. Mech. Phys. Solids 48 (4) (2000) 797–826.
[34] Huilong Ren, Xiaoying Zhuang, Hehua Zhu, Timon Rabczuk, Variational damage model: A novel consistent approach to fracture, Comput. Struct. 305 (2024) 107518.
[35] Huilong Ren, Timon Rabczuk, Xiaoying Zhuang, Variational damage model: A new paradigm for fractures, Front. Struct. Civ. Eng. 19 (1) (2025) 1–21.
[36] Christian Miehe, Martina Hofacker, Lisa-Marie Schänzel, Fadi Aldakheel, Phase field modeling of fracture in multi-physics problems. Part II. Coupled brittle-to-ductile failure criteria and crack propagation in thermo-elastic-plastic solids, Comput. Methods Appl. Mech. Engrg. 294 (2015) 486–522.
[37] Andro Mikelić, Mary F. Wheeler, Thomas Wick, A quasi-static phase-field approach to pressurized fractures, Nonlinearity 28 (5) (2015) 1371–1399.
[38] Mary F. Wheeler, Thomas Wick, Winnifried Wollner, An augmented-Lagrangian method for the phase-field approach for pressurized fractures, Comput. Methods Appl. Mech. Engrg. 271 (2014) 69–85.
[39] Blaise Bourdin, Chukwudi P. Chukwudozie, Keita Yoshioka, A variational approach to the numerical simulation of hydraulic fracturing, in: SPE Annual Technical Conference and Exhibition, Society of Petroleum Engineers, 2012.
[40] Huilong Ren, Xiaoying Zhuang, Yehui Bie, Timon Rabczuk, Hehua Zhu, Dual-horizon peridynamics-based variational damage modelling for complex dynamic fractures, Theor. Appl. Fract. Mech. 138 (2025) 104974.
[41] Yehui Bie, Xiangyang Cui, Zhoucheng Li, Abaqus implementation of dual peridynamics for brittle fracture, Comput. Methods Appl. Mech. Engrg. 330 (2018) 356–381.
[42] Dechun Lu, Xin Zhou, Xiuli Du, Guosheng Wang, 3D dynamic elastoplastic constitutive model of concrete within the framework of rate-dependent consistency condition, J. Engrg. Mech. 146 (11) (2020) 04020124.
[43] Dechun Lu, Fanping Meng, Xin Zhou, Yuhang Zhuo, Zhiwei Gao, Xiuli Du, A dynamic elastoplastic model of concrete based on a modeling method with environmental factors as constitutive variables, J. Engrg. Mech. 149 (12) (2023) 04023102.
[44] Dechun Lu, Xin Zhou, Jingyu Liang, Xiuli Du, Multi-physical and Non-orthogonal Geotechnical Plasticity Modeling and Algorithms, Springer Nature, 2025.

[45] Xin Zhou, Dechun Lu, Xiuli Du, Guosheng Wang, Fanping Meng, A 3d non-orthogonal plastic damage model for concrete, Comput. Methods Appl. Mech. Engrg. 360 (2020) 112716.
[46] Huilong Ren, Xiaoying Zhuang, Timon Rabczuk, A nonlocal operator method for solving partial differential equations, Comput. Methods Appl. Mech. Engrg. 358 (2020) 112621.
[47] Stewart A. Silling, Stability of peridynamic correspondence material models and their particle discretizations, Comput. Methods Appl. Mech. Engrg. 322 (2017) 42–57.
[48] Peng Li, Zhiming Hao, Wanqing Zhen, A stabilized non-ordinary state-based peridynamic model, Comput. Methods Appl. Mech. Engrg. 339 (2018) 262–280.
[49] Alan Arnold Griffith, The phenomena of rupture and flow in solids, Philos. Trans. R. Soc. Lond. Ser. A 221 (582–593) (1921) 163–198.
[50] George R. Irwin, Analysis of stresses and strains near the end of a crack traversing a plate, J. Appl. Mech. 24 (1957) 361–364.
[51] Kim Pham, Jean-Jacques Marigo, Corrado Maurini, Gradient damage models and their use to approximate brittle fracture, Int. J. Damage Mech. 20 (4) (2011) 618–652.
[52] Sanghyun Lee, Mary F. Wheeler, Thomas Wick, Pressure and fluid-driven fracture propagation in porous media using an adaptive finite element phase field model, Comput. Methods Appl. Mech. Engrg. 305 (2016) 111–132.
[53] Shuwei Zhou, Xiaoying Zhuang, Timon Rabczuk, A phase-field modeling approach of fracture propagation in poroelastic media, Eng. Geol. 240 (2018) 189–203.
[54] Shuwei Zhou, Xiaoying Zhuang, Timon Rabczuk, Phase-field modeling of fluid-driven dynamic cracking in porous media, Comput. Methods Appl. Mech. Engrg. 350 (2019) 169–198.
[55] Loup Verlet, Computer "experiments" on classical fluids. I. Thermodynamical properties of Lennard-Jones molecules, Phys. Rev. 159 (1) (1967) 98–103.
[56] Richard Courant, Kurt Friedrichs, Hans Lewy, On the partial difference equations of mathematical physics, IBM J. Res. Dev. 11 (2) (1967) 215–234.
[57] B.N. Biswas, Somnath Chatterjee, S.P. Mukherjee, Subhradeep Pal, A discussion on Euler method: A review, Electron. J. Math. Anal. Appl. 1 (2) (2013) 294–317.
[58] Hongwu Zhang, Hui Li, Hongfei Ye, Yonggang Zheng, Yixiong Zhang, A coupling peridynamic approach for the consolidation and dynamic analysis of saturated porous media, Comput. Mech. 64 (4) (2019) 1097–1113.
[59] Herbert F. Wang, Theory of Linear Poroelasticity with Applications to Geomechanics and Hydrogeology, Princeton University Press, 2000.
[60] R.Z. Ansari, R.T. Johns, Steady-state coning solutions with multiple wells and reservoir boundaries, in: SPE/DOE Symposium on Improved Oil Recovery, Society of Petroleum Engineers, 2006, pp. 1–10.
[61] Ian Naismith Sneddon, Morton Lowengrub, Crack Problems in the Classical Theory of Elasticity, John Wiley & Sons, 1969.
[62] Thierry Lhomme, C.J. De Pater, Peter Helfferich, Experimental study of hydraulic fracture initiation in Colton sandstone, in: SPE/ISRM Rock Mechanics Conference, Society of Petroleum Engineers, 2002.
[63] T.D. Cao, F. Hussain, Bernhard A. Schrefler, Porous media fracturing dynamics: Stepwise crack advancement and fluid pressure oscillations, J. Mech. Phys. Solids 111 (2018) 113–133.
[64] Changyi Yang, Fan Zhu, Jidong Zhao, A multi-horizon fully coupled thermo-mechanical peridynamics, J Mech.Phys. Solids 191 (2024) 105758.
[65] Changyi Yang, Fan Zhu, Jidong Zhao, Coupled total-and semi-lagrangian peridynamics for modelling fluid-driven fracturing in solids, Comput. Methods Appl. Mech. Engrg. 419 (2024) 116580.
[66] Changyi Yang, Jidong Zhao, Fan Zhu, Coupled thermo-hydrodynamic-mechanical peridynamics for thermal fluid-solid interactions with fracturing, J. Mech. Phys. Solids (2025) 106492.